# Journal Pre-proof

Thermo-hydrogen refinement of microstructure to improve mechanical properties of Ti-6Al-4V fabricated via laser powder bed fusion

Marko Knezevic, Saeede Ghorbanpour, Nicholas C. Ferreri, Iftekhar A. Riyad, Andelle D. Kudzal, James D. Paramore, Sven C. Vogel, Brandon A. McWilliams

PII: S0921-5093(21)00249-5

DOI: https://doi.org/10.1016/j.msea.2021.140980

Reference: MSA 140980

To appear in: Materials Science & Engineering A

Received Date: 9 January 2021
Revised Date: 12 February 2021
Accepted Date: 14 February 2021

Please cite this article as: M. Knezevic, S. Ghorbanpour, N.C. Ferreri, I.A. Riyad, A.D. Kudzal, J.D. Paramore, S.C. Vogel, B.A. McWilliams, Thermo-hydrogen refinement of microstructure to improve mechanical properties of Ti-6Al-4V fabricated via laser powder bed fusion, *Materials Science & Engineering A*, https://doi.org/10.1016/j.msea.2021.140980.

This is a PDF file of an article that has undergone enhancements after acceptance, such as the addition of a cover page and metadata, and formatting for readability, but it is not yet the definitive version of record. This version will undergo additional copyediting, typesetting and review before it is published in its final form, but we are providing this version to give early visibility of the article. Please note that, during the production process, errors may be discovered which could affect the content, and all legal disclaimers that apply to the journal pertain.

© 2021 Elsevier B.V. All rights reserved.



# Journal Pre-proof

Marko Knezevic

Conceptualization; Funding acquisition; Methodology; Project administration; Resources; Supervision; Data Curation; Roles/Writing – original draft; Writing – review & editing.

Saeede Ghorbanpour

Methodology; Formal analysis; Investigation; Visualization; Data Curation

Nicholas C. Ferreri

Methodology; Formal analysis; Investigation; Visualization

Iftekhar A. Riyad

Software; Formal analysis; Investigation; Visualization

Andelle D. Kudzal

Methodology; Formal analysis; Investigation; Visualization; Writing - Review & Editing

James D. Paramore

Methodology; Formal analysis; Investigation; Writing - Review & Editing

Sven C. Vogel

Methodology; Formal analysis; Investigation; Validation

Brandon A. McWilliams

Conceptualization; Funding acquisition; Project administration; Resources; Writing – review & editing.

# Thermo-hydrogen refinement of microstructure to improve mechanical properties of Ti-6Al-4V fabricated via laser powder bed fusion

Marko Knezevic<sup>a,\*</sup>, Saeede Ghorbanpour<sup>a</sup>, Nicholas C. Ferreri<sup>a</sup>, Iftekhar A. Riyad<sup>a</sup>, Andelle D. Kudzal<sup>b</sup>, James D. Paramore<sup>b,c</sup>, Sven C. Vogel<sup>d</sup>, and Brandon A. McWilliams<sup>b</sup>

#### **Abstract**

This paper describes the main results from an investigation into the consequences of thermohydrogen refinement of microstructure (THRM) after laser powder bed fusion (LPBF) of Ti-6Al-4V on the evolution of microstructure and mechanical properties using a set of experimental techniques. Porosity fraction, grain structure, phases, and crystallographic texture per phase are characterized using micro X-ray computed tomography, microscopy, and neutron diffraction. A hierarchical structure of acicular  $\alpha$ -phase morphology formed inside the prior  $\beta$  grains by fast cooling during LPBF transforms into fine-grained globular microstructure by THRM, which facilitates homogeneous nucleation and growth of the low temperature phase with some retained β phase. Moreover, hydrogenated material during THRM has low activation energy for diffusion, which in conjunction with the surface energy of pores causes densification of the material, thereby closing porosity formed during LPBF. Such significant microstructural changes induced by the THRM treatment cause brittle material created by LPBF to become ductile. Significantly, the strength and ductility produced by THRM exceed the minimums set forth by the ASTM B348 standard. Moreover, the treatment improves fatigue strength of the material. In particular, it improves the endurance limit and reduces the scatter in the measured fatigue strength data. Performance characteristics of the material can be further optimized for specific application requirements by tailoring microstructures using the LPBF and THRM processes.

*Keywords*: Microstructures; Texture; Hydrogen; Additive manufacturing; Heat Treatment; Ti-6Al-4V

<sup>&</sup>lt;sup>a</sup> Department of Mechanical Engineering, University of New Hampshire, Durham, NH 03824,

<sup>&</sup>lt;sup>b</sup> Weapons and Materials Research Directorate, DEVCOM Army Research Laboratory, Aberdeen Proving Ground, MD 21005, USA.

<sup>&</sup>lt;sup>c</sup> Department of Metallurgical Engineering, University of Utah, Salt Lake City, UT 84112 <sup>d</sup> Materials Science and Technology Division, Los Alamos National Laboratory, Los Alamos, NM 87545, USA.

<sup>\*</sup> Corresponding author: <u>marko.knezevic@unh.edu</u> (Marko Knezevic).

#### 1. Introduction

Alloy Ti-6Al-4V (Ti64) shows a range of desirable properties such as high stiffness to weight ratio, static strength, fatigue strength, and toughness as well as excellent corrosion resistance for various applications, particularly in aerospace, marine, and medical industries [1-3]. Microstructures of Ti64 alloy consist of hexagonal close-packed (HCP) α-phase and bodycentered cubic (BCC) \(\beta\)-phase, whose fraction, shape, and distributions can substantially vary and, as a result, properties can be designed towards particular applications [4]. A variety of microstructures can be achieved in Ti64 by variation in processing from wrought to powder metallurgy to additive manufacturing (AM) and subsequent heat treatments [5-8]. AM has attracted major attention due to its capability to build parts with complex geometries through a layer-by-layer approach. Additionally, AM ensures high material utilization and a near-net-shape without the need for molds and other tooling [9-11]. Consequently, a substantial amount of research is being devoted to AM [12-18], and in particular, to AM of Ti64 to possibly achieve better buy-to-fly ratios [19]. The repetitive melting and solidification along with heating and cooling during AM processing forms microstructures different from traditional manufacturing methods [20]. In the case of Ti64, the microstructure consists of fine  $\alpha$  lath (acicular) structure [21-24]. These lath structures shorten mean-free path of gliding dislocations. As a result, the material is very strong and brittle. AM metals usually have higher tensile strength compared with conventional metals. However, AM-created defects significantly compromise ductility and, in particular, the fatigue strength [25]. To make AM metals qualified for industrial use, improvements in terms of material behavior are needed. High porosity, poor surface finish, and tensile residual stresses cannot merely be eliminated by establishing optimal AM processing windows in conjunction with in-situ process monitoring/control [20, 26-30]. As a result, the structure of AM metals must be modified by subsequent heat treatments or other post-processing methods such as hot isotropic pressing (HIP), laser shock peening, machining, laser polishing, etc. These methods decrease porosity, improve surface finish, and reduce tensile residual stresses. This paper is concerned with evaluating the evolution of microstructure and mechanical properties of Ti64 produced by laser powder bed fusion (LPBF) subjected to thermo-hydrogen refinement of microstructure (THRM) post-processing treatment.

The process of THRM is based on a powder metallurgy (PM) process called hydrogen sintering and phase transformation (HSPT) [5], and shares two of the same inventors [31, 32]. PM is a beneficial method for Ti alloys production since it reduces the costs compared to the wrought material due to its near-net-shape capabilities [5, 33]. However, PM Ti64 components typically have inferior mechanical properties compared to wrought counterparts [33]. Either pre-alloying the powder and/or pressure-assisted sintering processes and/or subsequent thermo-mechanical processing are usually applied to improve the mechanical properties of PM Ti64, which significantly increase the cost [7, 34]. HSPT was developed as a method for producing high performance and wrought-like Ti64 using only low energy/cost feedstocks and processing. It is three-step process that uses dynamically controlled H<sub>2</sub> partial pressures to achieve accelerated densification and microstructure engineering [5-7]. The first step is  $\beta$ -Ti(H) sintering, in which the presence of hydrogen lowers the  $\beta$  transus temperature and increases concentration of vacancies in Ti64. These effects achieve increase in substitutional diffusion of Ti and the alloying elements, allowing > 99% densification to occur under moderate temperatures and times. During the second step, hydrogen-enabled phase transformations are used to refine the microstructure, resulting in an ultrafine-grained microstructure of lamellar  $\alpha$  colonies and very

finely dispersed retained β. The last step of HSPT is dehydrogenation under vacuum or inert gas to remove residual hydrogen to < 10 ppm [5-7]. Subsequently, the material can be heat treated to produce a range of fine wrought-like globularized, bi-modal, or lamellar microstructures [35]. During wrought processing, such microstructural engineering requires significant deformation energy via mechanical working to drive recrystallization. However, the microstructural evolution in HSPT Ti64 is driven by the large degree of grain boundary energy in the ultrafine-grained microstructure. This allows wrought-like microstructures to be produced without mechanical working, which is energy-intensive. Similar hydrogen-enabled processing has been used to improve near-net-shape cast components [36, 37].

THRM was developed as a heat treatment for bulk components that uses the same underlying mechanisms as HSPT. The key advantages of the THRM treatment are healing defects (e.g. pores) and producing wrought-like microstructures from essentially any starting condition through the hydrogen-enabled mechanisms. Driven by the surface energy, microstructural pores/cracks can close due to the enhanced diffusivity in the presence of hydrogen. We show here that THRM can be used as a post-process for bulk titanium products produced by AM. Importantly, AM process induced porosity heals without requiring applied pressure through processes like HIP. Defects are healed due to enhanced titanium self-diffusion produced by the presence of relatively weak Ti-H bonds, which is driven by the surface energy resulting from the presence of pores and cracks. As such, process induced defects are healed without requiring applied pressure. Likewise, traditional thermomechanical processing relying on the plastic deformation and recrystallization of microstructure can be circumvented. We use THRM to improve the microstructure and properties of Ti64 components produced by LPBF. To this end, strength in tension and compression, ductility, and high cycle fatigue strength are measured for samples of Ti64 created by LPBF followed by stress relieving (SR) and a set of samples which subsequently underwent the THRM treatment. The behavior is rationalized and explained using microstructural characterization data represented in terms of porosity fraction, grain structure, phases, and crystallographic texture per phase. The characterization was performed using micro X-ray computed tomography (µXCT), microscopy, and neutron diffraction (NeD) for samples before and after THRM.

## 2. Material and experiments

2.1 Fabrication via laser powder bed fusion (LPBF) and subsequent thermo-hydrogen refinement of microstructure (THRM)

Bulk specimens in the form of cylinders were built from gas atomized powder of Ti64 supplied by 3D Systems, Rock Hill, SC using a 3D Systems model ProX300 metal laser powder bed fusion (LPBF) additive manufacturing machine in an ultra-high purity (99.999%) argon atmosphere. Distribution of powder particle size is given in Fig. 1. Processing parameters were as follows: laser power = 275 W; laser speed = 1800 mm/s; hatch spacing = 85  $\mu$ m, layer thickness = 40  $\mu$ m. Parts were stress relieved (SR), while still attached to the build platform, using a thermal cycle of 4 hours at a temperature of 600 °C in an argon atmosphere. Stress relieving was necessary before cutting the parts off the plate to prevent cracking and distortion during removal. Following the stress relief treatment, the samples were electric discharge machined (EDM) from the build platforms. Following the removal, half of the samples were

treated by thermo-hydrogen refinement of microstructure (THRM). The remaining half were tested and characterized in the SR state. These samples are termed as as-built + SR.

During the first step of THRM (Fig. 2 - I), the sample is heated to a temperature well above the  $\beta$ -transus under a hydrogen-containing atmosphere. For the LPBF samples processed in this study, a temperature of 1050 °C for 1 hour and a 50.7 kPa (50% atmospheric pressure) partial pressure of H<sub>2</sub> was used. It should be noted that, due to the fact that hydrogen lowers the  $\beta$ -transus temperature, even lower temperatures may be used in the first step, which may also produce smaller and more desirable prior  $\beta$  grains.

During the second step of THRM (Fig. 2 - II), the material is cooled to below the β-transus and held for several hours to allow for phase transformation. The phase transformation step used in this study was 650 °C for 4 hours. In a traditional super-transus heat treatment,  $\alpha+\beta$  alloys (e.g. Ti64) will undergo heterogeneous nucleation of  $\alpha$  phase along the parent  $\beta$  grain boundaries upon cooling, which grow into the  $\beta$  grains with a  $\{110\}_{\beta} || \{0001\}_{\alpha}$  and  $\langle 1\bar{1}1\rangle_{\beta} || \langle 11\bar{2}0\rangle_{\alpha}$ Burgers relationship [35]. This produces colonies of coarse lamellar  $\alpha$  grains that are crystallographically parallel, and share slip systems across an entire colony. Furthermore, only a few colonies of  $\alpha$  grains can form from each prior  $\beta$  grain, meaning the average unimpeded slip path length is on the same scale as the prior  $\beta$  grain size. However, the presence of hydrogen during THRM and HSPT causes (Ti-6Al-4V)-xH to act as a metastable β alloy [38, 39]. As such, the material undergoes homogeneous nucleation of  $\alpha_2$  (Ti<sub>3</sub>Al) and  $\alpha$  when cooled below the  $\beta$ transus, producing  $\alpha$  colonies two orders of magnitude finer than the prior  $\beta$  grains. It is believed that this is enabled by a spinodal decomposition of the prior  $\beta$  grains, similar to what is observed in other metastable  $\beta$  alloys [35]. This hypothesis is based on observations of  $\beta$  peak splitting during in situ synchrotron X-ray diffraction in an HSPT study [38, 39]. As the material is cooled further, it undergoes a eutectoid decomposition around 200 °C, whereby some of the remaining β phase transforms into  $\alpha$  and  $\delta$  (TiH<sub>2</sub>) grains, further refining the microstructure.

The process of pore closure in a partial pressure of hydrogen during THRM is attributed to improved diffusion by introduction of the relatively weak Ti-H bonds. Hence, hydrogen lowers the activation energy of diffusion enough that the surface energy penalty produced by the pores is enough to drive further densification of the material, thereby closing porosity. Mechanistically, the process is identical to the third stage of sintering in a powder metallurgy process, and hydrogen is well-know to improve densification of Ti alloys during sintering. The main purpose of the phase transformations that occur during THRM is to refine the microstructure, by enabling homogenous nucleation of the low temperature phases. The ultrafine-grained microstructure that is produced by homogenous nucleation has enough grain boundary energy, in turn, to enable formation of globularized or bi-modal microstructures, which govern a range of properties to be produced.

Hydrogen, which is well known to severely embrittle Ti alloys, is removed during the third step of THRM (Fig. 2 - III) by annealing the material under a sufficiently hydrogen-free atmosphere (inert gas or vacuum). Dehydrogenation must be done at a low enough temperature to prevent coarsening of the microstructure. In this study, a dehydrogenation temperature of 750 °C for 12 hours under high vacuum ( $<10^{-3}$  Pa) was used. This results in a hydrogen concentration less than 10 ppm in the final part, which is overkill with regards to hydrogen embrittlement. Shorter dehydrogenation times or more economical atmospheres, such as rougher vacuum ( $\sim10^{-1}$  Pa) or inert gas, will produce a <100 ppm hydrogen concentration [40], which is still well below the

ASTM standard for any grade of wrought Ti64 (150 ppm) [41]. As such, the time and atmosphere used in this study are not economically optimized. The removal of hydrogen causes all the  $\delta$  phase and most the  $\beta$  phase to transform into  $\alpha$ . Furthermore, as the  $\alpha$  phase fraction increases, all  $\alpha_2$  transforms into  $\alpha$ . This is because  $\alpha_2$  is simply an ordered form of  $\alpha$  that is produced by supersaturation with Al. The result of this step is a unique ultrafine grained lamellar microstructure, with  $\alpha$  colonies orders of magnitude finer than the prior  $\beta$  grains and a small fraction of ultrafine retained  $\beta$  grains confined to the triple points of the  $\alpha$  colonies.

After dehydrogenation, the material was subjected to a sub-transus heat treatment similar to those used in wrought processing (Fig. 2 - IV). This was done by heating the material to 950 °C for 1 hour under high vacuum ( $<10^{-3}$  Pa) and furnace cooling ( $\le 10$  °C/min) to room temperature. At the heat treatment temperature, the  $\alpha$  colonies produced during THRM coalesce, driven by the large amount of grain boundary energy due to the ultrafine grain size. Furthermore, the  $\beta$  grains grow to accommodate approximately 60 vol% of the microstructure. This produces a mixture of relatively equiaxed  $\alpha$  and  $\beta$  grains at the heat treatment temperature. As the material is slowly cooled, the  $\beta$  grains recede to the triple points of the  $\alpha$  grains produced both at the heat treatment temperature and during cooling [5]. The resulting microstructure is similar to a fully globularized/equiaxed microstructure produced by wrought processing, but without any mechanical working. In this microstructure, the  $\alpha$  grains have an average size of about 4-8  $\mu$ m.

The final step used in this study was an aging treatment (Fig. 2 - V) to boost strength while retaining ductility by causing nucleation of secondary  $\alpha$  and  $\alpha_2$  grains. In this study, an aging treatment of 550 °C for 6 hours under high vacuum was used. It is possible that the aging temperature used in this study was likely high to promote the greatest strength. This is because the solvus temperature for  $\alpha_2$  is 550 °C. Therefore, aging treatments of Ti64 are typically performed at temperatures below 540 °C to encourage formation of  $\alpha_2$  [42]. As such, further work is needed to determine if additional strength could be achieved in THRM-processed materials through an improved aging treatment.

For this study, a heat treatment was chosen that produces a globularized microstructure that maximizes ductility. This was done as LPBF Ti64 has very poor ductility. Therefore, it was hypothesized that the starkest improvement in performance would be gained by producing this microstructure. We point out that by changing the dehydrogenation temperature in step III, the cooling rate used in step IV, and other parameters, a range of microstructures and corresponding properties can be produced. As such, this post-process can be used to tailor the properties to specific application requirements.

All THRM processing in this study was done in a custom-built tube furnace with a 100 mm ID x  $\sim$ 305 mm L hot zone. H<sub>2</sub> partial pressures were produced by flowing mixtures of ultrahigh purity (99.999%) Ar and H<sub>2</sub> gases at atmospheric pressure ( $\sim$ 101 kPa) using digital mass flow controllers (Aalborg GFC). High vacuum was produced using an oil diffusion pump (Edwards Diffstak 100/300). Diffusion pumps have significantly faster H<sub>2</sub> pumping speeds than the alternatives (e.g. turbomolecular pumps), which is beneficial for dehydrogenation.

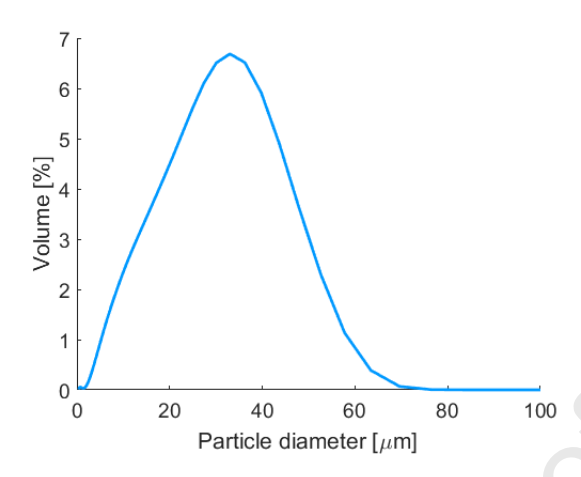


Figure 1. Particle size distribution via laser diffraction. Mean particle size is approximately 26 µm.

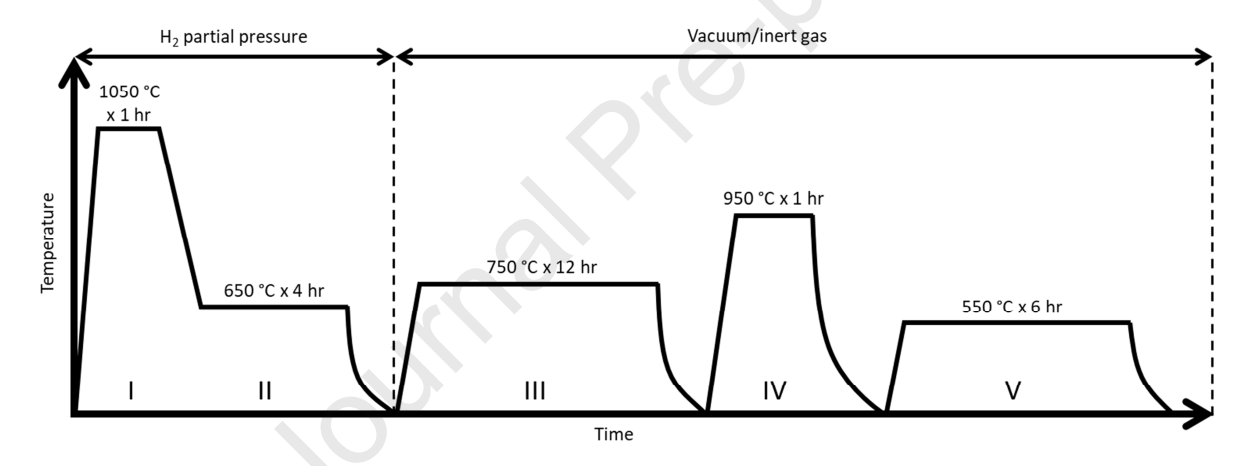


Figure 2. Schematic of the five step THRM profile used in this study (not to scale), consisting of (I) hydrogen charging and microstructure reset, (II) phase transformation and refinement, (III) dehydrogenation, (IV) globularization, and (V) aging.

# 2.2 Microstructural characterization procedures

To verify successful LPBF and characterize porosity fraction in samples of Ti64, micro X-ray computed tomography ( $\mu$ XCT) imaging was performed using a Zeiss Xradia 520 Versa Micro CT. The applied voltage on the tungsten source tube of the instrument was 90 kVp and 77.3  $\mu$ A for collecting images. The images were collected using the 0.4X Olympus objective achieving a voxel size at the sample of 3.6  $\mu$ m. The tomograms were reconstructed and rendered using Ziess' reconstruction software, and analyzed using Bruker's CTAn software. While voxel size defines the measurement resolution, a reliable measurement of a void requires multiple voxels [43, 44].

To further investigate microstructure in the materials, microscopic characterization was performed. Metallographic specimens were sectioned with a high speed metallographic saw and

hot/compression mounted in a conductive graphite-impregnated phenolic resin. Upon mounting, the samples were ground with 180 grit followed by 320 grit SiC paper (ANSI). After grinding, the samples were polished with 9 and then with 3 µm glycol diamond suspension. Finally, the samples underwent an "attack polish" with 3 parts, by volume, 0.05 µm colloidal-silica to 1 part 30 % H<sub>2</sub>O<sub>2</sub>. Samples meant for optical microscopy were etched using Kroll's Reagent (2 parts, by volume, HF, 3 parts HNO<sub>3</sub>, and 95 parts H<sub>2</sub>O) for 3-5 s. This etchant is known for revealing the structure of Ti64. Optical images were taken using a confocal Keyence VK X-200 microscope. Sample preparation for electron backscattered diffraction (EBSD) included mechanical grinding on abrasive paper up to 800 grit and subsequent electrochemical polishing. The polishing was performed in 1 M ethylene glycol (C<sub>2</sub>H<sub>6</sub>O<sub>2</sub>)-sodium chloride (NaCl) electrolyte solution [45] at 24 V and room temperature for 30-40 minutes until mirror finish of the surface is obtained. Details of this novel sample prep for Ti and alloys have been described in [46]. Tescan Lyra SEM with EDAX EBSD system was used for the scanning at 20 kV. Multiple scans were taken from different areas of samples with every scan containing around 500,000 points to ensure statistically significant data. A coarse step size of 3-4 µm was used for coarse scans. Since no microstructural morphology can be observed in these coarse scans, these scans were used to determine prior  $\beta$  grain size and obtain texture. Additionally, high resolution EBSD scans were performed to better reveal structure in the materials.

Neutron diffraction (NeD) experiments were performed on the time-of-flight high-pressure-preferred orientation (HIPPO) neutron diffractometer at the pulsed neutron source of the Los Alamos Neutron Science Center (LANSCE) at Los Alamos National Laboratory [47]. Ti64 samples were orientated such that the build direction was perpendicular to the incident neutron beam. Count time was equivalent to approximately 30 min at a proton current of 100  $\mu$ A. In total, 132 histograms were obtained from three different sample orientations (0°, 67.5°, and 90°) for the five HIPPO detector rings with nominal diffraction angles of 150°, 120°, 90°, 60°, and 40°. The 132 histograms were used to calculate an orientation distribution function (ODF) and were also integrated to create single histograms for each neutron diffraction angle that are largely free from texture influence. The Maud diffraction analysis software was used to obtain all experimental neutron diffraction histograms [48].

#### 2.3 Mechanical testing procedures

Monotonic tensile tests were performed on specimens prepared according to ASTM E8/E8M [49]. A slight modification on the gripping portions is introduced to facilitate mounting using a pair of flat grips. Drawing of the tensile sample is given in the Appendix. To perform the tensile tests, a biaxial MTS servo hydraulic machine with Flextest software and controller with a loading capacity of 250 kN was employed. A one-inch MTS 623.12E-24 extensometer was attached to the gauge section of the samples during the tests to gather the displacement data. The data from the extensometer was used for obtaining stress-strain curves. The tensile tests were done at room temperature and a strain rate of  $\sim 10^{-3}$ /s. The tests were continued until fracture. The tests were repeated per sample category at least two times to assure the repeatability and accuracy. The curves overlapped.

Compression tests were performed on cylinders of 7.5 mm in diameter and 10 mm in height. To perform these tests, an Instron 1350 machine with a load cell capacity of 100 kN equipped with the DAX software and controller was used. The cylindrical specimen was placed between two

grounded and polished dies made of hardened steel. To ensure that the loading is uniaxial as much as possible, a hardened steel ball was placed between the upper force arm and the die. Molykote (primarily composed of  $MoS_2$ ) was used to minimize the friction between the specimen and the upper/lower compression dies. Prior to testing of the samples, the compliance of the machine and testing setup was measured. The compliance data was used to correct the compression testing data before calculating the true stress-true strain curves [50-52]. All the tests with Instron 1350 were done at a strain rate of  $10^{-3}$  /s and at room temperature. For repeatability of the data, compression tests were repeated at least three times for each category (Appendix). The tests were continued until the specimens broke.

For the load reversal tests, the specimens were designed according to ASTM E606/E606M [53]. The drawing is given in the Appendix. Similar to the tensile samples, a slight modification was applied to the gripping region for mounting purposes. The same MTS machine was used for the strain-controlled load reversal tests at room temperature and under a strain rate of  $10^{-3}$  /s. During the tests, an MTS 632.26E-40 axial extensometer was attached to the gauge section of the specimens to measure the elongation. These tests start from zero strain, the samples are pulled to a specific level of strain, and then unloaded and deformed in the reverse direction to zero strain. The next stage of the loading starts from the zero strain level and the procedure of loading/unloading repeats. These tests were repeated two times to ensure the accuracy of the results. Excellent repeatability was achieved.

High cycle fatigue specimens were designed according to the ASTM E466-15 [54-56]. The drawing is given in the Appendix. An RBF-40HT rotating beam tester machine was employed to perform the HCF tests in the air at room temperature. The machine has a counter to shows the number of cycles during testing. The tests were fully-reversed (R = -1) stress-controlled with the stress ranging between 250 MPa and 1010 MPa. The frequency was kept at 50 Hz. The tests were not interrupted until the specimens failed or they reached the endurance limit, which is taken to be  $10^7$  cycles.

#### 3. Results

## 3.1 Microstructural characterization

The visual representations of porosity in the samples is given in Fig. 3. The purpose of these measurements was to verify quality of the builds and determine the effect of THRM. The samples imaged by  $\mu XCT$  were machined cylinders. The measured height for the as-built + SR sample was 2.17 mm with the diameter of 3.20 mm. The measure height for the THRM sample was 2.68 mm with the diameter of 3.20 mm. Area fraction of defects along the height of the cylinders from recorded 2D images is also provided. The as-built + SR sample found several instances of layers with large concentrations of defects as high as 0.6%, while the THRM specimen had less detected porosity with a max layer wise porosity of 0.12%. The  $\mu XCT$  determined porosity fractions in the as-built + SR and THRM materials are 0.13455% and 0.03128%, respectively. Minimum detectable defects were limited to greater than 260  $\mu m^3$  detection limit. While majority of defects in the as-built + SR material were smaller than 2,000  $\mu m^3$ , the average was 10,000  $\mu m^3$ , largely owing to a few defects as large as 200,000  $\mu m^3$ . A total of about 2,300 defects were identified in the imaged volume for the as-built + SR material. Defects in the THRM material were much smaller. Significantly, the THRM reduces the fraction

of porosity/defects for approximately 5x. Small gas pores and delaminations due to lack of fusion caused by insufficient consolidation of the powder particles (incomplete powder coverage) are expected to be primary contributors to the porosity fraction [57]. However, the gas pores are harder to detect via µXCT due to their size.

Fig. 4 shows optical micrographs of as-built+SR and THRM Ti64 samples. In the optical images,  $\alpha$  is the light phase, while  $\beta$  is the dark phase. The fine features are also shown in the high resolution EBSD scans in Fig. 5. The grain tolerance angle used to define the grains from the EBSD analysis was set to 5°. When Ti64 is cooled rapidly from  $\beta$  phase, the formation into  $\alpha$ from  $\beta$  may be martensitic, or occur by nucleation and growth. Both pathways are capable of forming a microstructure consisting of fine, interpenetrating  $\alpha$  laths with lack of grain boundary a. Such microstructures are referred to as fine basket weave, Widmanstätten, or fine lath. It is worth noting that the morphology only is insufficient to describe the  $\alpha$  phase as martensitic [58]. However, Ti does not derive its strength from the tetragonal distortion of the cubic lattice like in the case of steels. Instead, the strength is governed from the effective dislocation mean-free-path and slip transfer of the dislocations and, thus, whether or not AM microstructures are formed by martensitic or nucleation dominated and growth mediated diffusional processes is inconsequential. In summary, as-built + SR Ti64 is a heterogeneous material with a complex acicular/ lath structure formed inside the chessboard  $\beta$  structure. In contrast, the structure of THRM Ti64 consists of the primary α phase grains, which are globularized to have a relatively low aspect ratio and some retained β. Such microstructure is achieved by slow cooling rate, where the  $\beta$  grains transform into globularized  $\alpha$  microstructure. Prior  $\beta$  grain size was ~200 µm, which is easy to determine due to the presence of grain boundary  $\alpha$  along prior  $\beta$  grain boundaries. While this grain boundary α is known to affect fatigue performance to some degree, it has little to no effect on static properties. The globularized  $\alpha$  grains measure about 4  $\mu$ m by 8 μm, on average i.e. are slightly elongated (less than 3:1 aspect ratio on average).

Fig. 6 depicts measured coarse IPF maps. These maps are used to obtain IPF maps of β grains and determine texture of the  $\beta$ -phase. Results of the reconstruction are shown in the figure. The average size of the prior  $\beta$  grains is approximately  $a = 80 \mu m$ ,  $b = 80 \mu m$ , and  $c = 460 \mu m$ . For completeness, a procedure for constructing prior  $\beta$  grains from discrete EBSD scan data is briefly summarized.  $\alpha$ -variants belonging to a given  $\beta$  grain are related by their Burgers relation, which places a given crystallographic plane/line of one phase into the alignment with plane/line of the other phase [59]. These are:  $\{110\}_{\beta} \| \{0001\}_{\alpha}$  and  $\langle 1\bar{1}1\rangle_{\beta} \| \langle 11\bar{2}0\rangle_{\alpha}$  along with their habit planes:  $\{11\ \overline{11}\ 13\}_{\beta}$ ,  $\{4\ 4\ \overline{5}\}_{\beta}$ , and  $\{3\ 3\ \overline{4}\ \}_{\beta}$  [60-63]. 12 crystal orientations/variants of  $\alpha$  could be obtained from one parent  $\beta$  grain during  $\beta \to \alpha$  transformation. However, only 6 orientations of  $\beta$  can be produced form one  $\alpha$  variant during  $\alpha \to \beta$  transition [64-67]. If we define a rotation tensor rotating a sample frame into the crystal lattice frame for a  $\beta$  parent grain as **G** and the 24 cubic crystal symmetries as  $\mathbf{S}_{i}^{\beta}$  then  $\mathbf{S}_{i}^{\beta}\mathbf{G}$  makes 24 symmetries of one parent  $\beta$  grain. The Burgers relation  $\mathbf{D}$  can be expressed using Bunge-Euler angles as  $\mathbf{D} = (135^{\circ}, 90^{\circ}, 354.74^{\circ})$  [64, 68]. As a result of  $\mathbf{DS}_{i}^{\beta}\mathbf{G}$ , the orientations of 24  $\alpha$  variants are created. Of these, 12  $\alpha$ orientations are unique due to the commutation property of **D**. For the  $\alpha \to \beta$  transformation, 6  $\beta$ variants are produced from one  $\alpha$  orientation. A parent  $\beta$  grain can be identified from a minimum of 3 inherited  $\alpha$  variants. However, certain combinations may not yield a unique solution due to a  $\{111\}$  mirror plane in the  $\beta$  phase. To avoid this non uniqueness, 4 unique variants are recommended [69]. More details can be found in the following works [64, 65, 68].

The particular method used in the present work is the code reported in [70]. In this method, pixels are segmented into  $\alpha$  colonies based on a 2° misorientation tolerance. Every  $\alpha$  lath variant is evaluated, one at a time, with its nearest neighbors as potentially be from the same  $\beta$  grain. The misorientation between the given primary lath and each immediate neighbor are compared with allowed misorientations for two variants from the given  $\beta$  grain. After 4 unique  $\alpha$  variants are found, we calculate the 6 parent  $\beta$  grain orientations that could form the established variants. We then calculate the misorientation between the 6 possible solutions for the primary  $\alpha$  lath and the 6 possible solutions for each of the neighbors. Finally, the angles of misorientation between all of the possible solutions are then checked to obtain the  $\beta$  grain orientation that is common among them.

Figure 7 shows the integrated histograms for all samples from the 150° detector bank. The phase composition of each sample was determined by fitting the corresponding integrated experimental neutron diffraction histogram and calculating the diffraction contribution for each phase. The Rietveld method was applied whereby the relevant crystallographic and scaling parameters of all phases were refined to increase the quality of the least-squares fit between calculated and experimental diffraction histograms. The procedure follows that presented in [71]. Table 1 shows the phase compositions per sample. Any β contribution to the observed NeD signal was indistinguishable from background noise for the as-built + SR materials, which indicates the lack of presence or, at most, trace quantities of β. These measurements confirm that rapid heating/cooling conditions during LPBF create an entirely  $\alpha$  structure with only traces of  $\beta$  [24]. Some fraction of the β-phase is present in the THRM samples.

Pole figures showing texture in the samples are presented in Figs. 8-10. Thse pole figures are plotted from the ODFs calculted with NeD data. Initial texture and texture evolution under compression for the as-built + SR samples in shown in Fig. 8. Similarly, the initial texture and texture evolution for  $\alpha$ -phase under compression for the THRM samples is shown in Fig. 9. Textures in Figs. 8 and 9 are remarkably similar, although phase transformations took place in evolving texture from the material in Fig. 8 to the material in Fig. 9 by THRM. Fig. 10 shows pole figures for the  $\beta$ -phase obtained by NeD and by  $\beta$ -phase reconstruction. Despite the large sampling volume afforded by NeD,  $\beta$ -phase low volume fraction likely resulted in the undersampling of  $\beta$  grains, which could have created the higher pole density seen in Fig. 10a than in Fig. 10b. Nevertheless, the two methods of determining texture of the  $\beta$ -phase crossvalidated one another.

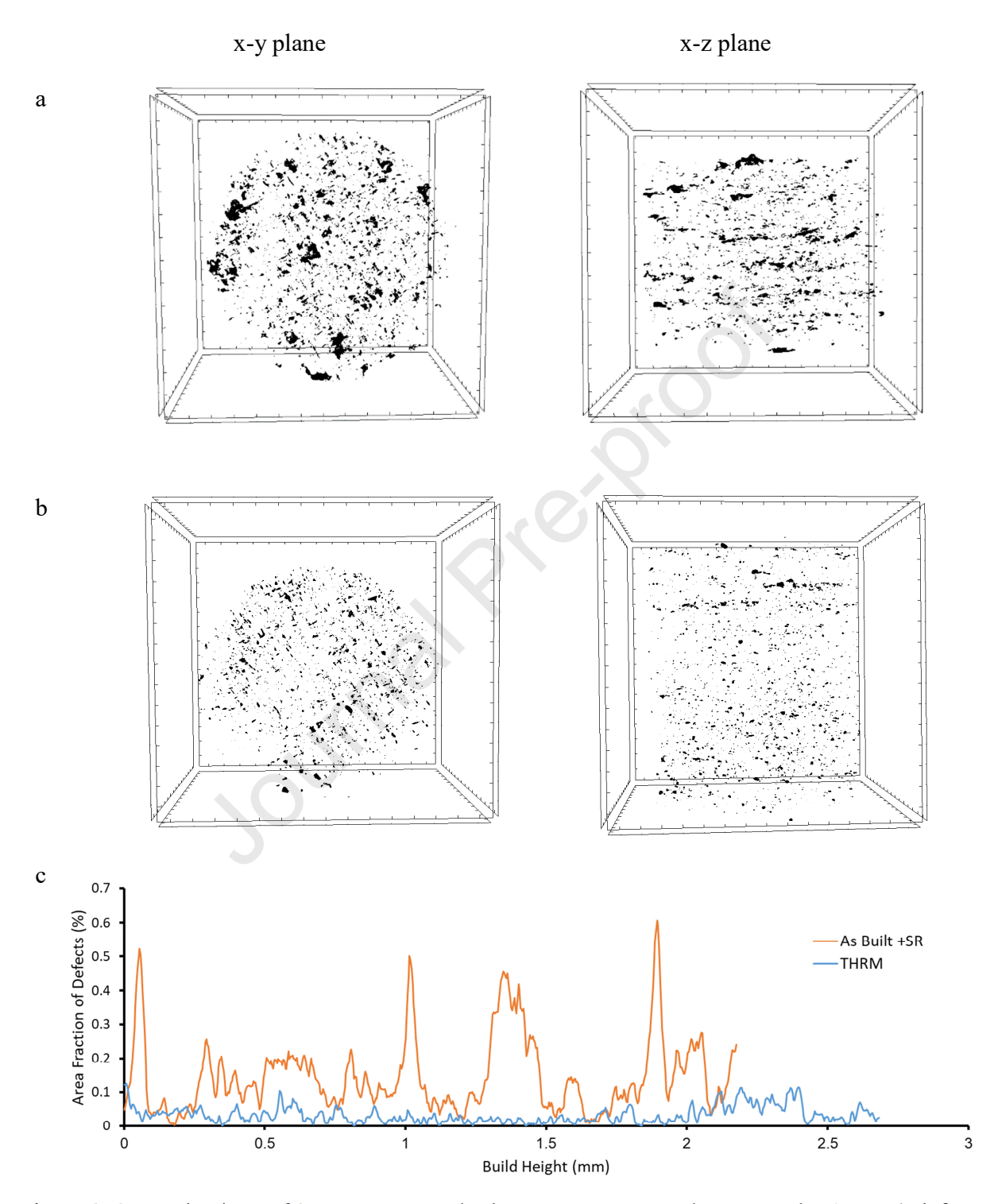


Figure 3. 2D projections of 3D reconstructed micro X-ray computed tomography ( $\mu$ XCT) defect analysis on (a) as-built + SR (for 4 h at 600 °C under Ar) and (b) THRM Ti64 alloy given in x-y and x-z planes. Spacing between tick lines is 250  $\mu$ m. (c) Area fraction of defects along height of the cylinders from recorded 2D images.

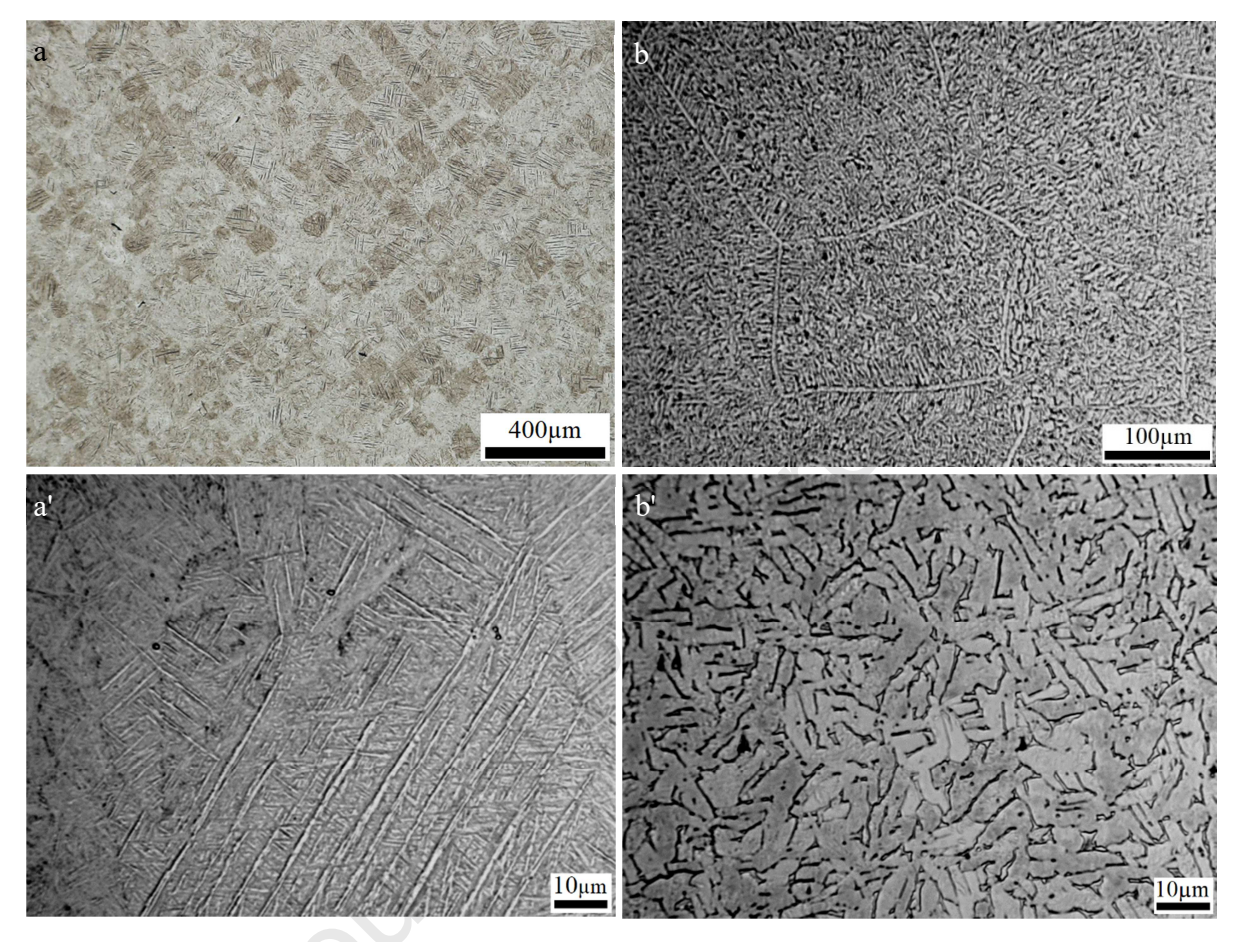


Figure 4. Optical microscopy images of (a, a') as-built + SR and (b, b') HT. The build direction is perpendicular to the micrographs.

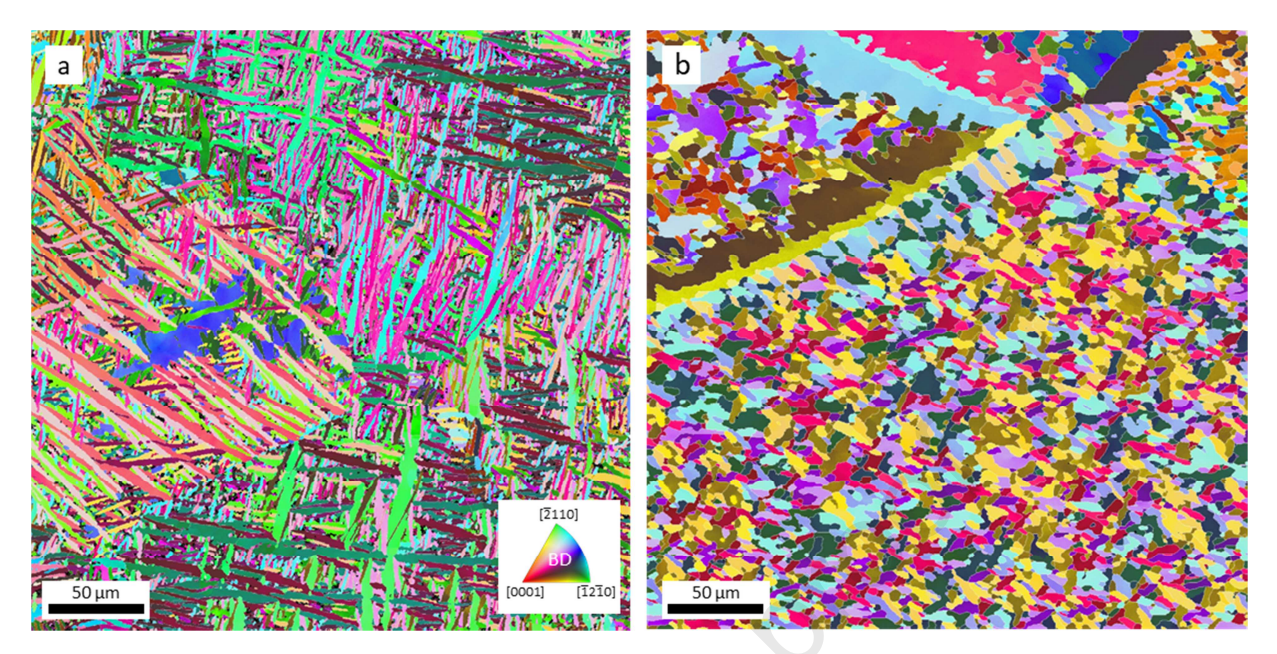
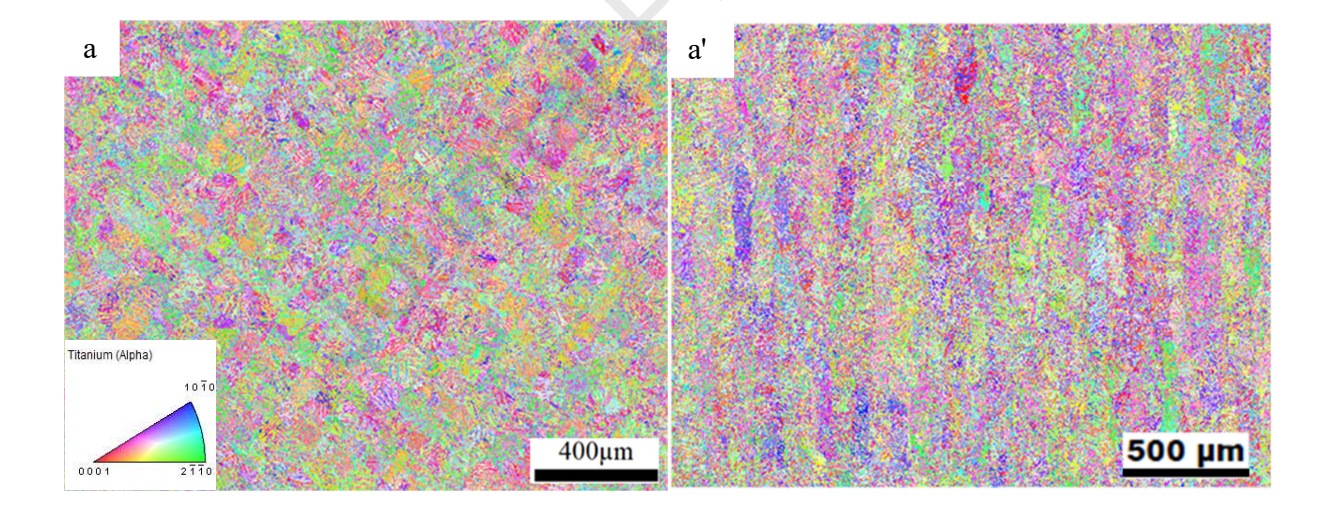


Figure 5. IPF maps showing the initial structure for: (a) as-built + SR and (b) THRM Ti64 with build direction (BD) out of plane.



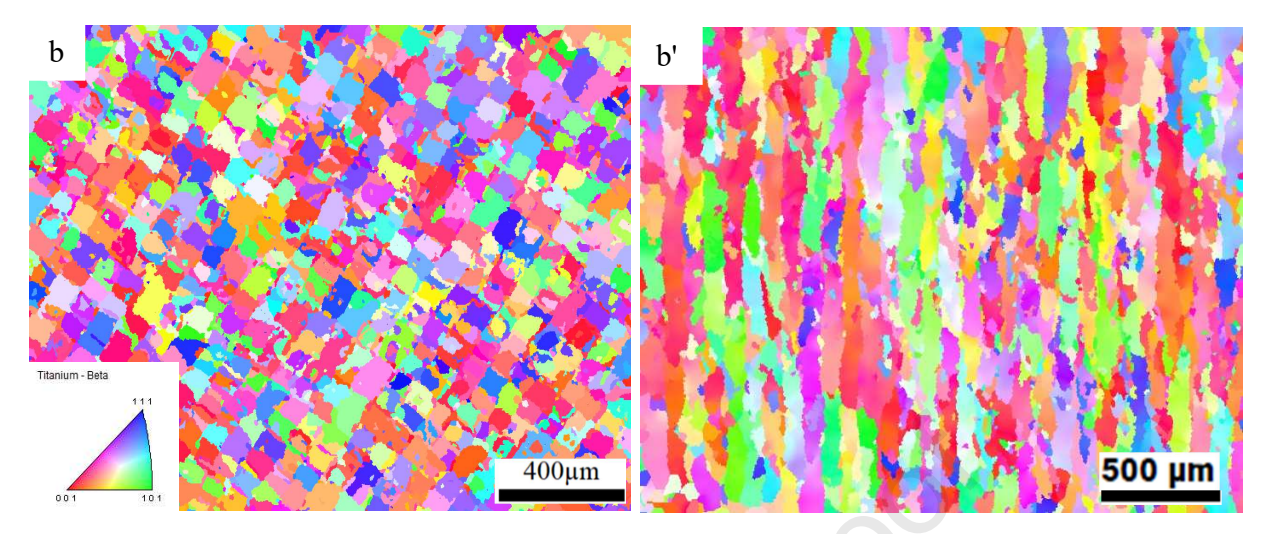


Figure 6. (a) and (a') IPF maps measured by EBSD and (b) and (b') corresponding reconstructed maps of  $\beta$  grains in Ti64 fabricated via LPBF. The build direction (BD) is perpendicular to the unprimed, while the BD is vertical for the primed images. The colors in the maps define the BD relative to the crystal lattice frame according to the standard triangles provided in the corners.

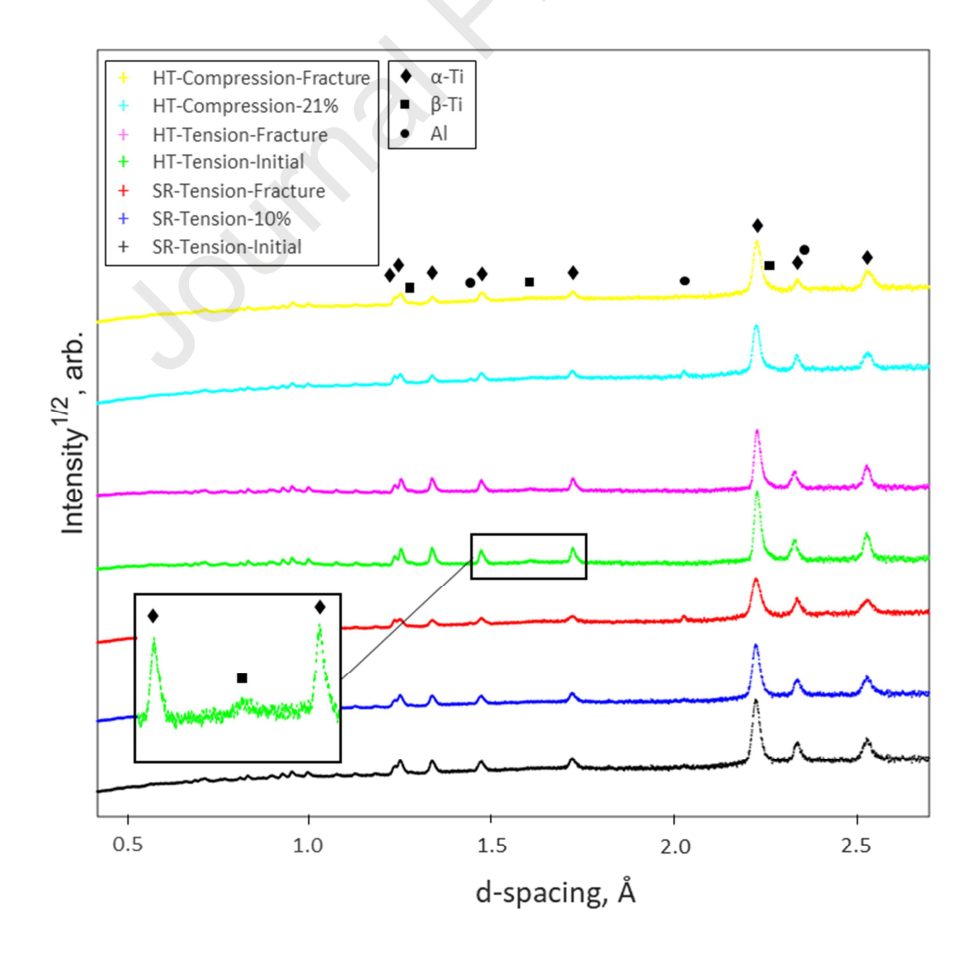


Figure 7. Experimental neutron diffraction histograms from the 150° detector bank for all studied conditions of Ti64. Bragg reflections for  $\alpha$  and  $\beta$  phases are labeled except for those with low d-spacings or intensities near background, which were omitted to enhance plot readability. Inset shows  $\beta$  reflection for undeformed SR tensile sample. Metallic aluminum (Al) reflections were seen because of neutron beam interaction with Al sample holders, which resulted in the occasional detection of Al-diffracted neutrons in the 150° detector banks.

Table 1. Phase Volume Fractions as determined from NeD.

	α-Ti	β-Ті	
SR-Compression-initial	100 %		
SR-Compression-0.09	100 %	<del>(</del> 0	
SR-Compression-fracture	100 %	<b>)</b> .	
HT-Tensile-initial	95.9 %	4.1 %	
HT-Tensile-fracture	94.6 %	5.4 %	
HT-Compression-0.21	96.1 %	3.9 %	
HT-Compression-fracture	95.7 %	4.3 %	

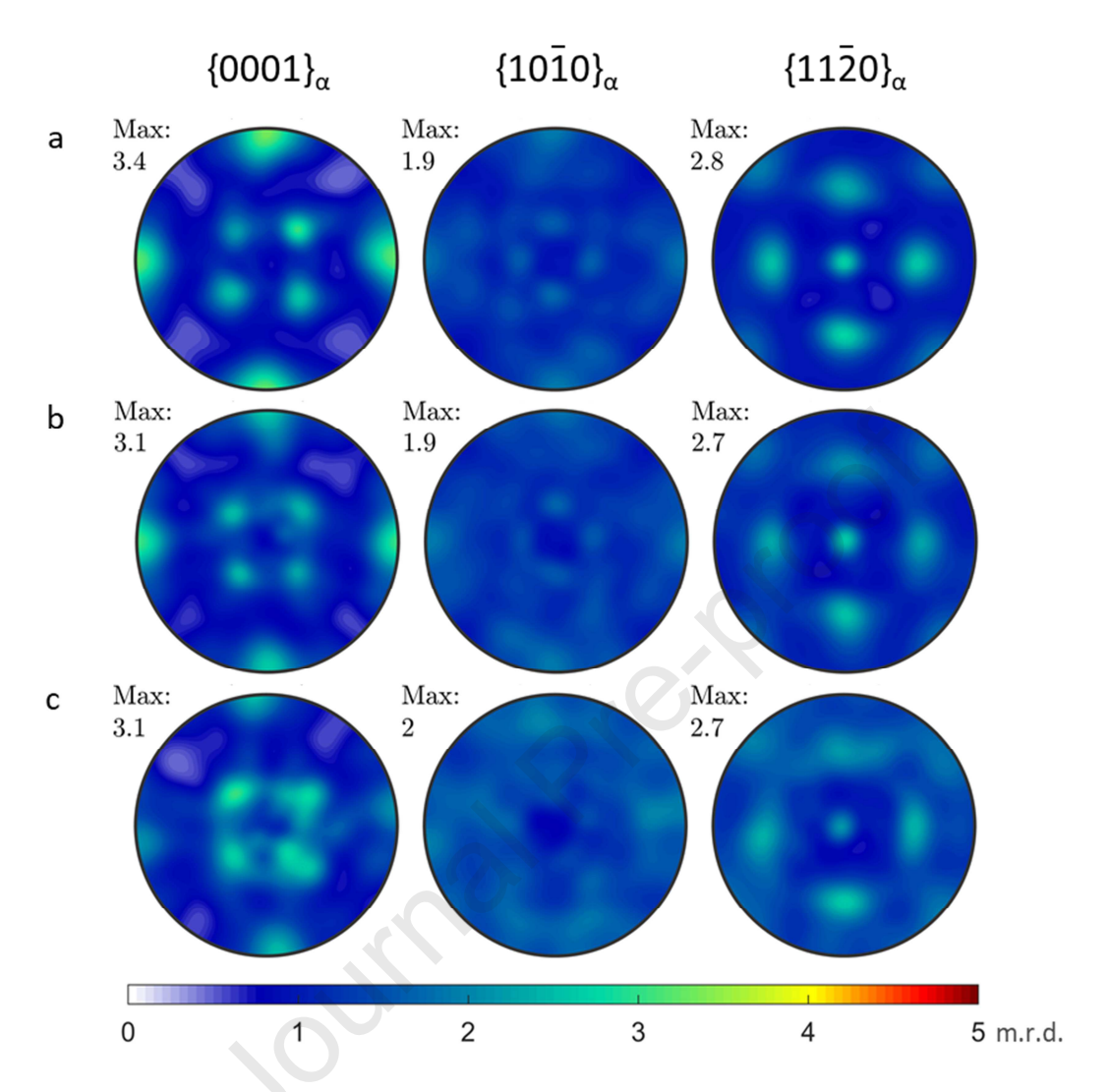


Figure 8. Stereographic pole figures obtained by neutron diffraction for samples of as-built + SR material: (a) initial, (b) deformed in compression to a strain of 0.09, and (c) deformed in compression to fracture. Build direction is pointing out of the plane.

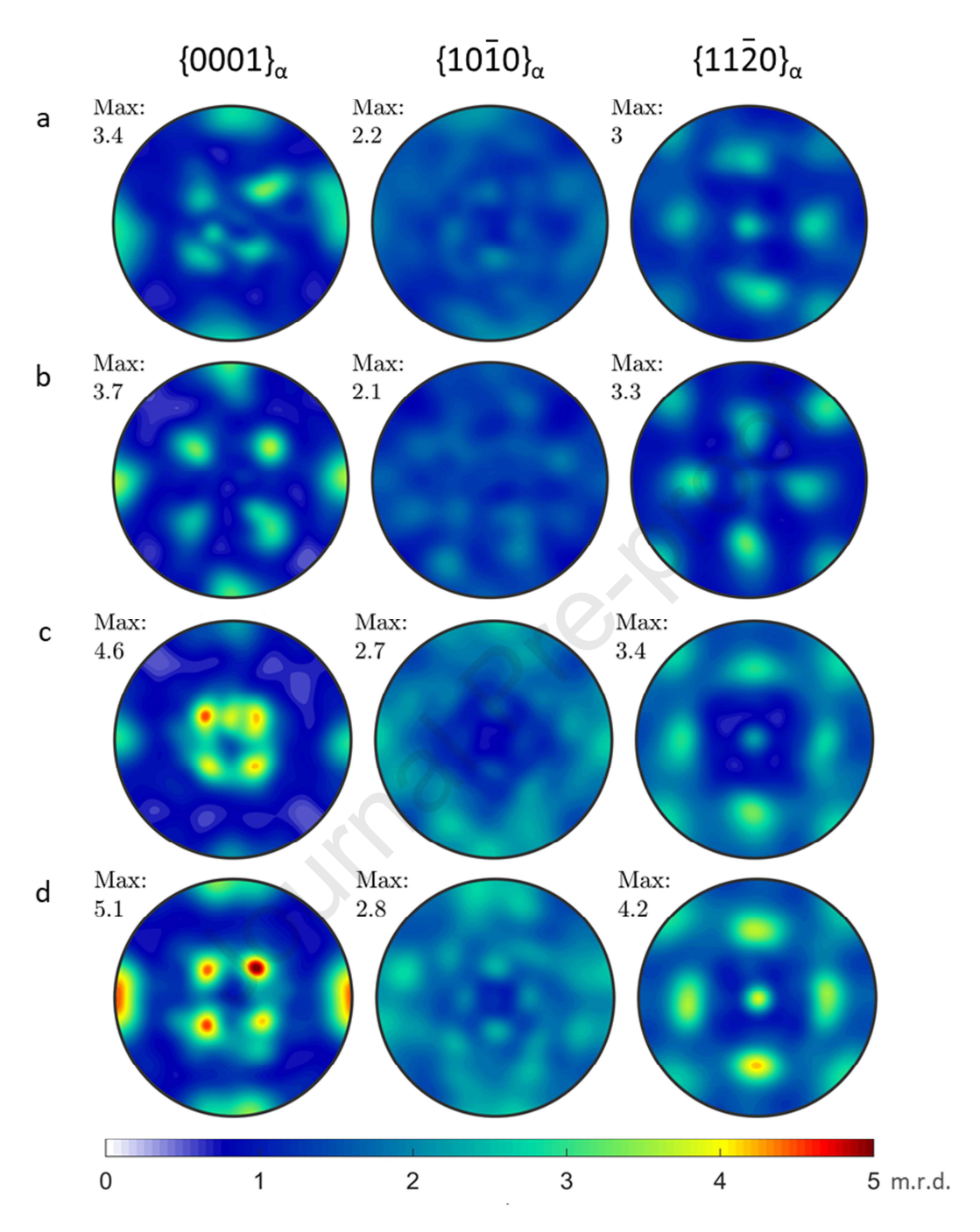


Figure 9. Stereographic pole figures obtained by neutron diffraction for samples of THRM material: (a) initial, (b) pulled in tension to fracture, (c) deformed in compression to 0.21, and (d) deformed in compression to fracture. Build direction is pointing out of the plane.

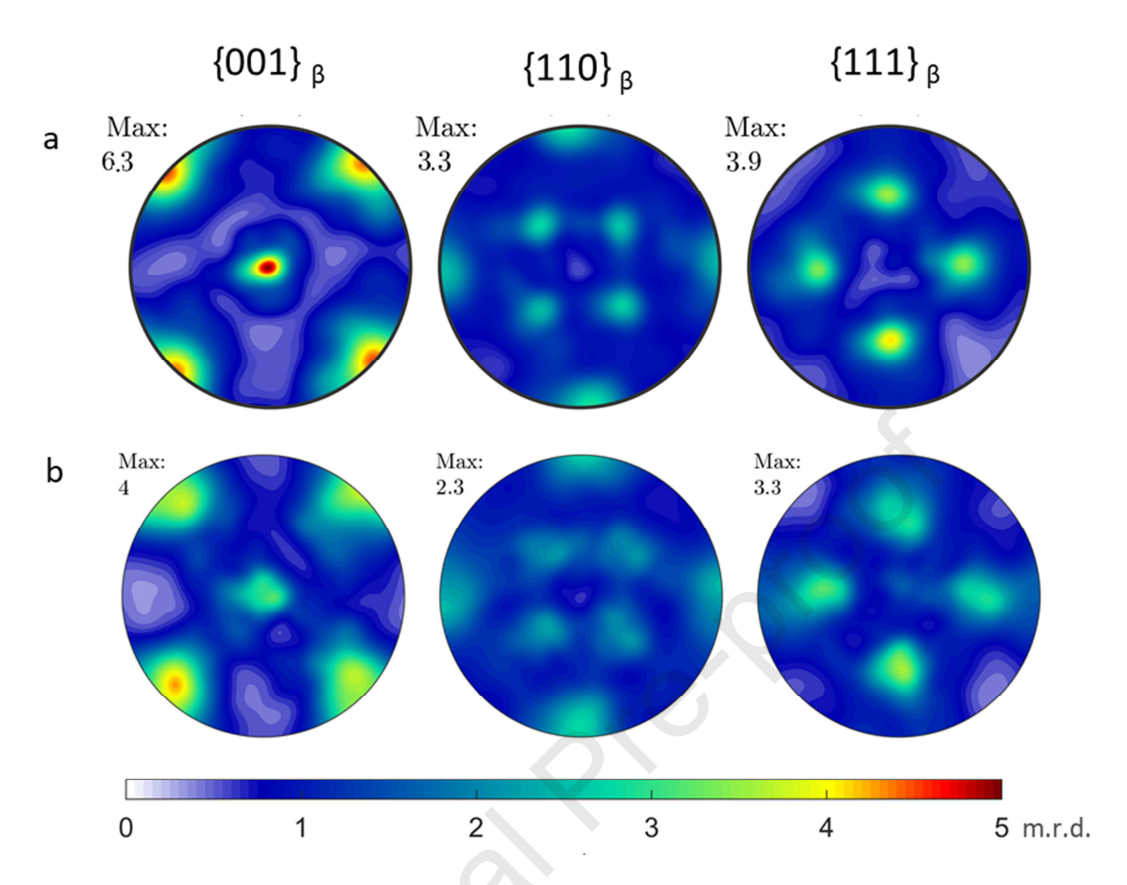


Figure 10. Stereographic pole figures for  $\beta$  phase obtained by (a) neutron diffraction and (b) grain reconstruction for THRM initial samples. Build direction is pointing out of the plane.

## 3.2 Mechanical testing

We now turn our attention on the results correlating the structures and properties of Ti64. Strength in tension and compression are measured at room temperature under 0.001 /s strain rate for the two material conditions. True stress—strain and engineering stress-strain curves in tension and compression for the two conditions are given in Fig. 11. The compressive curves are provided in two sample directions, along the BD and perpendicular to it. Table 2 summarizes quantitative values of the main material properties. As is evident, the THRM treatment has a noticeable effect on the mechanical properties. While the as-built + SR material is stronger, the THRM material is significantly more ductile. Properties of the latter material are greater than the minimums set forth by the ASTM B348 standard [41]. Interestingly, the material in both conditions exhibits some tension/compression (T-C) asymmetry, being stronger in compression than in tension. The as-built + SR flow curved have been used in the recent modeling work [72].

Fig. 12 shows the stress–strain curves for the as-built + SR and THRM samples, when the samples are first pre-loaded in tension to certain strains. The test are carried out for one or multiple cycles. As can be seen, the THRM material can afford larger strains and more cycles than the as-built + SR material. The as-built + SR material breaks before even reaching a true pre-strain of 0.03. These plots show phenomena pertaining to the cyclic deformation of the

materials including the non-linearity of unloading, the Bauschinger effect, and any changes in hardening rates during reverse loading from those reached during forward loading. At the onset of unloading, the material exhibits some linear portion and prolonged non-linear portion until next yielding. The extent of non-linearity increases with the amount of pre-strain. Fig. 12c shows that the THRM material yields at a slightly lower value of stress in compression than reached during the tensile pre-strain. The yield differential is referred to as the Bauschinger effect [73-79]. The differential is influenced by the T-C asymmetry (Fig. 11) i.e. the material is stronger in compression, which compensates for the larger extent of the Bauschinger effect.

Fig. 13 presents the stress amplitude vs. the number of cycles to failure (S – N or  $\sigma_a - N_f$ ) measured data for as-built + SR and THRM samples of Ti64. The arrows indicate that the particular test was halted at  $10^7$  cycles before the sample failed. The lines in the plots are fits of the discrete points for the fractured specimens (Table 3). These fitted lines are extrapolated to the intersection with the horizontal line indicating the endurance limit. The data follows typical trends of  $N_f$  increasing with a decrease in  $\sigma_a$ .  $R^2$  values characterizing the quality of the fits are also provided. As is evident, the HCF behavior of samples after THRM is better than those as-built + SR, except for the very high stress amplitudes. This is attributed to the higher strength of the as-built + SR material. The results clearly show that it is possible to improve the fatigue strength of Ti64 by THRM. The globularized  $\alpha$  grain structure with some porosity after THRM can better suppress fatigue crack initiation than the acicular  $\alpha$  structure with a larger content of porosity before THRM. The improvements vary with  $\sigma_a$  and are the greatest at the endurance limit. Significantly, the endurance limit improved from 285 MPa to 400 MPa (Table 2). Moreover, the scatter in the measured fatigue strength data significantly reduced.

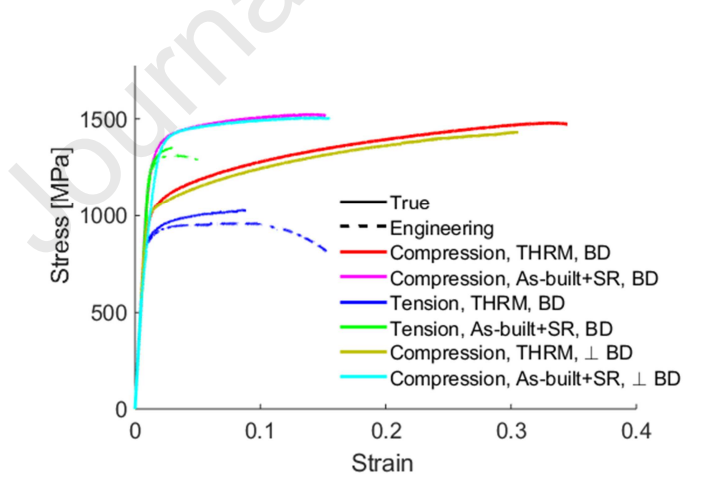


Figure 11. True stress-strain curves for as-built + SR and THRM samples of Ti64 in compression and tension along BD at room temperature tested at a strain rate of 10<sup>-3</sup>/s. Engineering stress-strain curves for the tensile tests are also shown.

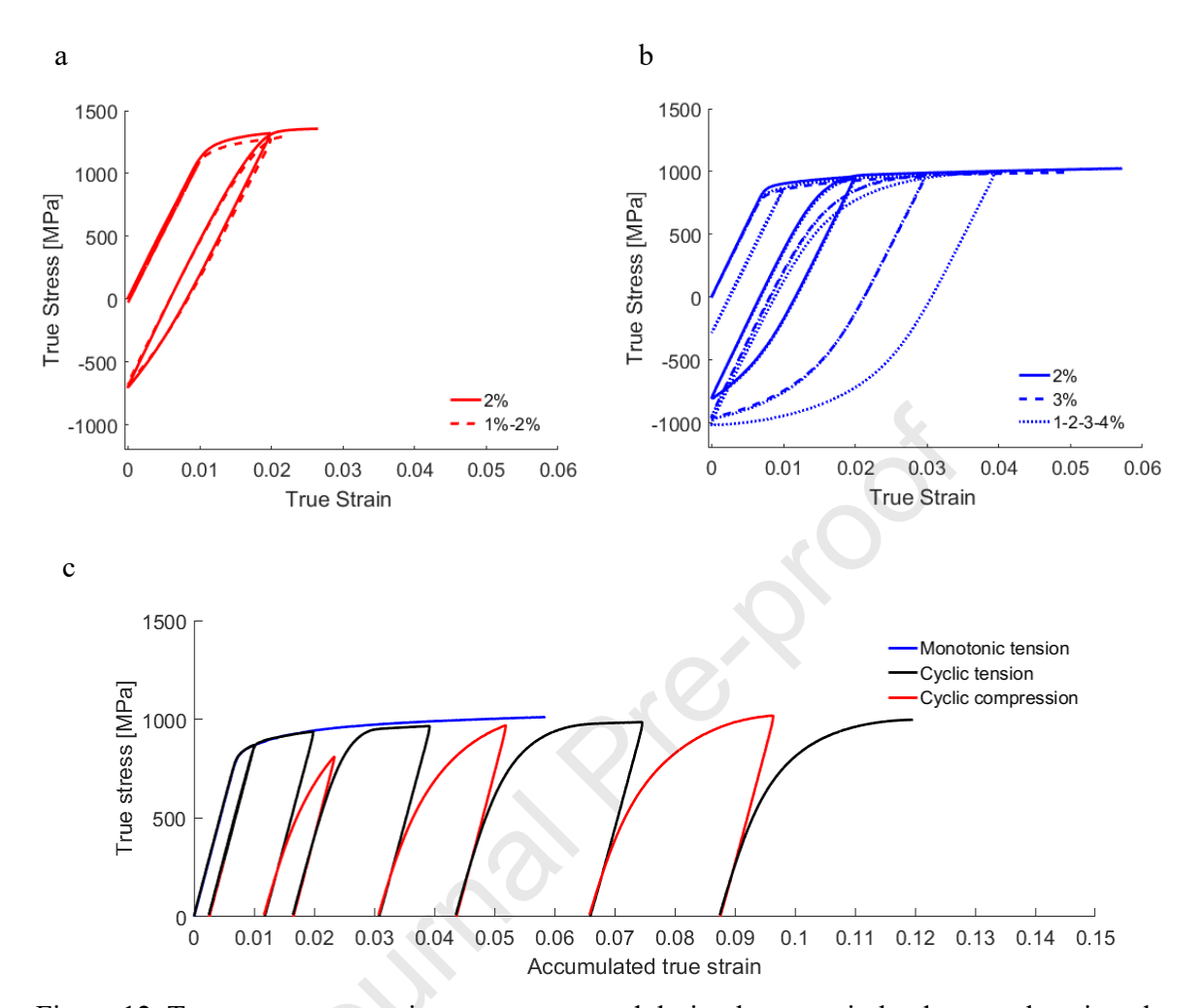


Figure 12. True stress-true strain curves measured during large strain load reversal testing along the BD: (a) as-built + SR and (b) THRM Ti64 alloy. The strain values indicated in the legends refer to the pre-strained increments. (c) True stress-accumulated true strain curves for the THRM 1%-2%-3%-4% sample.

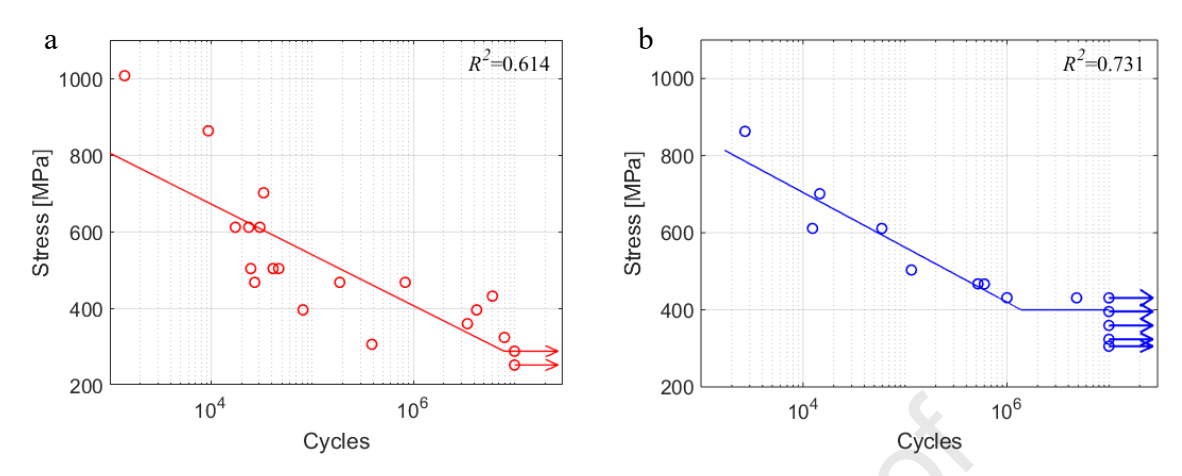


Figure 13. HCF behavior of (a) as-built + SR and (b) THRM Ti64 tested along the built direction at room temperature. The rotating beam tester imposes the *R*-ratio ( $\sigma_{\min}/\sigma_{\max}$ ) of -1.

Table 2. Summary of measured properties based on Figs. 11 and 13 for the two categories of Ti64 samples.

Material	Yield strength (0.2% offset) [MPa]	Ultimate tensile strength (UTS) [MPa]	Strain at fracture	Fatigue strength at 10 <sup>7</sup> [MPa]
As-built + SR	1250	1310	0.050	285
HT	860	950	0.164	400

Table 3. High cycle fatigue data fit parameters for  $A \log(N) + B$  equations.

Material	A	В
THRM	-145.33	1286.5
As-built + SR	-104.15	1041.8

#### 4. Discussion

In this work, it is demonstrated that THRM is well-suited for improving the microstructure and properties of Ti64 samples produced by LPBF. Tensile/compressive strength, ductility, and high cycle fatigue strength are measured for samples of Ti64 created by LPBF after stress relieving (SR) and after the THRM treatment. The testing results show that the SR samples exhibit higher strengths but substantially lower ductility and fatigue strength compared with the THRM samples. Therefore, the THRM treatment improves ductility, toughness, and fatigue strength. The material in both conditions exhibits some T-C asymmetry, being stronger in compression than in tension. Higher strength in compression is beneficial for fatigue performances. Literature suggests that the resolved shear stress on the pyramidal slip systems in Ti64 is dependent not only on the stress in the direction of slip but also on the two orthogonal shear stress components and the three normal stress components (non-Schmid effects) [80-88]. These non-Schmid effects may be a source of the observed T-C asymmetry in the studied materials. Additionally, the

source of T-C asymmetry can be a higher propensity for cross slip when titanium alloys are deformed in tension, which was reported in [89]. The load reversal tests reveal that the T-C asymmetry reduces the Bauschinger effect, which is usually present during cyclic deformation. In addition to the poor fatigue strength exhibited by the as-built + SR material, sample-to-sample variability is another major issue for using such material for stringent fatigue sensitive applications. Large scatter in AM fatigue data has also been observed in [90]. The THRM process reduces the scatter. The degree by which scatter was reduced by THRM varies with  $\sigma_a$  and the greatest reduction in scatter was observed at the endurance limit. Significantly, the endurance limit improved from 285 MPa to 400 MPa. However, the as-built + SR behaves better for the very high stress amplitudes. This is attributed to the higher static strength of the asbuilt + SR material. The fatigue performance of a material is often judged by the ratio between the fatigue strength at endurance and the static UTS. Such comparison makes the effect of THRM even more apparent since the ratio significantly improves.

Microstructural features for samples of LPBF Ti64 were measured before and after THRM to infer the role these features have in governing the set of measured mechanical properties of the materials. The microstructural characterization data in terms of porosity fraction, grain structure, phases, and crystallographic texture per phase were collected using µXCT, microscopy, and NeD. It was found that the fine  $\alpha$  lath microstructure resulting from fast cooling during LPBF, in conjunction with some porosity, makes Ti64 very brittle. As discussed earlier, α laths are crystallographically correlated, allowing for slip transfer among α laths to accommodate plasticity, which has been demonstrated experimentally in titanium alloys [91-94]. Given the extremely short mean-free-path for mobile dislocations in the fine as-built + SR microstructure, the material is very strong but not ductile. Similar observations have been reported in the literature [95, 96]. While it may be possible to slightly improve the properties by LPBF process optimization [97], we show that post-treatments are a better path forward. This work has explored the effect of THRM, which facilitates the formation of wrought-like microstructures through hydrogen-enabled phase transformations. Moreover, the presence of hydrogen increases diffusion kinetics of the material, allowing pore closure during THRM. THRM significantly reduced the overall fraction of porosity as well as the average pore size. The globularized  $\alpha$  grain structure with some porosity after THRM can better suppress fatigue crack initiation than the acicular α structure with a larger content of porosity before THRM. While grain structure between as-built + SR and THRM samples is substantially different, crystallographic texture is remarkably similar for  $\alpha$ -phase. Therefore, it is inferred that texture introduces only secondary effect on the properties. Fraction of β-phase is not sufficient to introduce any appreciable influence of texture on the properties.

Since the total volume of pores measured throughout the samples with the given resolution was negligible, we regard our LPBF of Ti64 as successful. Nevertheless, the measurements show presence of some residual porosity even in the THRM samples. The estimates are regarded as lower bound of the total porosity in the material because some small gas pores were not resolved. While these smaller pores would likely not have appreciable effect on static strength, ductility and fatigue strength are likely affected. Methods such as HIP and gaseous isostatic forging (GIF) can be explored to further improve fatigue performances of the THRM treated material. GIF is process that relies on rapid heating and isostatic pneumatic pressure [98]. Data showing the effects of GIF on removing the residual porosity of HSPT-sintered Ti64 and improving fatigue properties exist in the literature [5]. Therefore, combining THRM with another treatments such

as GIF could ultimately produce porosity-free Ti64 with wrought-like microstructures and properties.

In closing, we show several fractography images for samples broken in simple tension and HCF. Fig. 14 shows secondary electrons (SE) images of fractured surfaces for samples of as-built + SR and THRM materials tested to fracture in tension. A typical cup and cone fracture can be observed for both materials. The rim areas of both conditions show relatively flat trans-granular fracture. The interior surface of the as-built + SR fractured sample exhibits surface facets and some inter lamellar character, where  $\alpha$  laths are often visible on the quasi-cleavage surfaces. These quasi-cleavage facets are  $\alpha$  grains broken in a planar manner. Such features are more representative of brittle mode than ductile mode of fracture [3]. Conversely, dimples that are typical of microvoid coalescence dominate the THRM sample surface. These dimples correlate with the much more ductile behavior of the THRM material than the as-built + SR material. Fractured surfaces of the HCF specimens (Fig. 15) appear much smoother than the tensile fracture surfaces. The largest stress develops at the surface of the sample in a rotating beam test. The surface stress linearly decreases to zero towards the sample center. Therefore, initial crack/cracks usually form at the surface. Fatigue surfaces of the as-built + SR sample exhibit surface facets, but to a smaller degree than after simple tension. Additionally, the fatigue crack path propagated along defects produced by lack of fusion during LPBF (Fig. 15- a"). These insufficient fusion of layers (delamination) defects formed during AM appear to contribute much more to the porosity fraction than gas pores. Unmolten particles can be observed on the smooth surfaces of the insufficient fusion of layers defects. The presence of these defects has greatly reduced after THRM. The topology of the THRM fatigue sample also includes fatigue striations (1-2 µm spacing), which developed as a consequence of crack blunting and reshaping during fracture propagation. Such features were not observed in the as-built + SR samples, suggesting that the sample likely fractured more rapidly after crack initiation due to its brittleness.

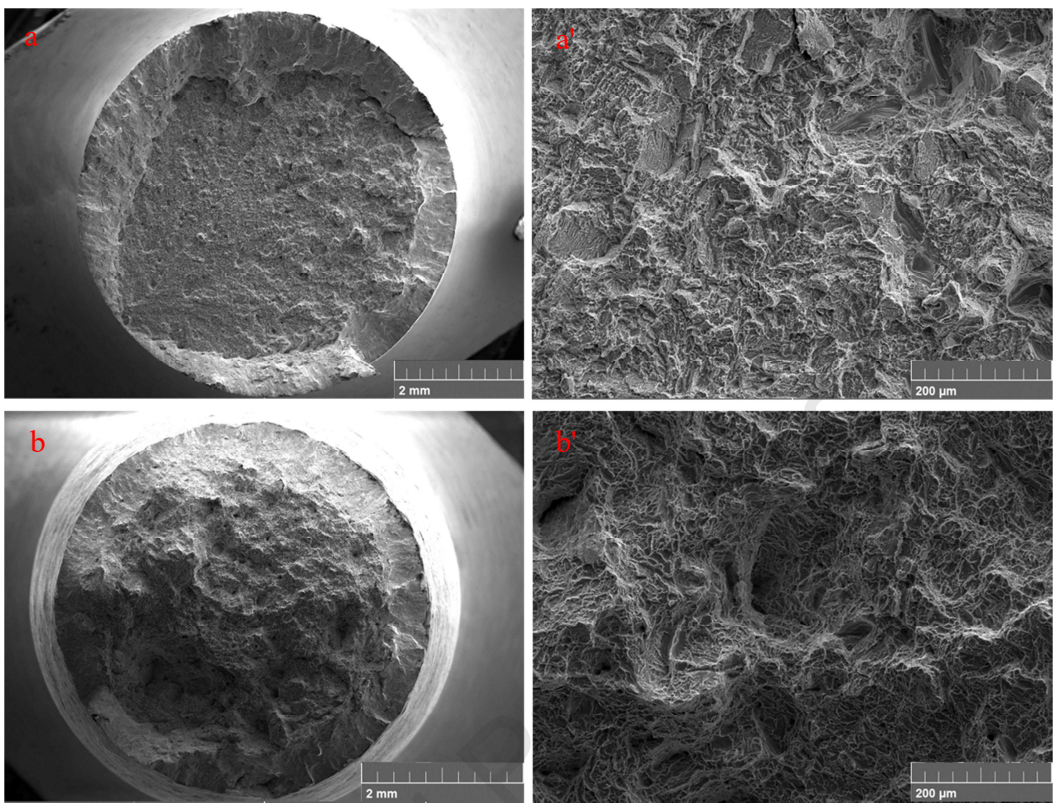


Figure 14. SE images of fractured surfaces for samples tested to fracture in simple tension: (a and a') as-built + SR (top row) and (b and b') THRM (bottom row).

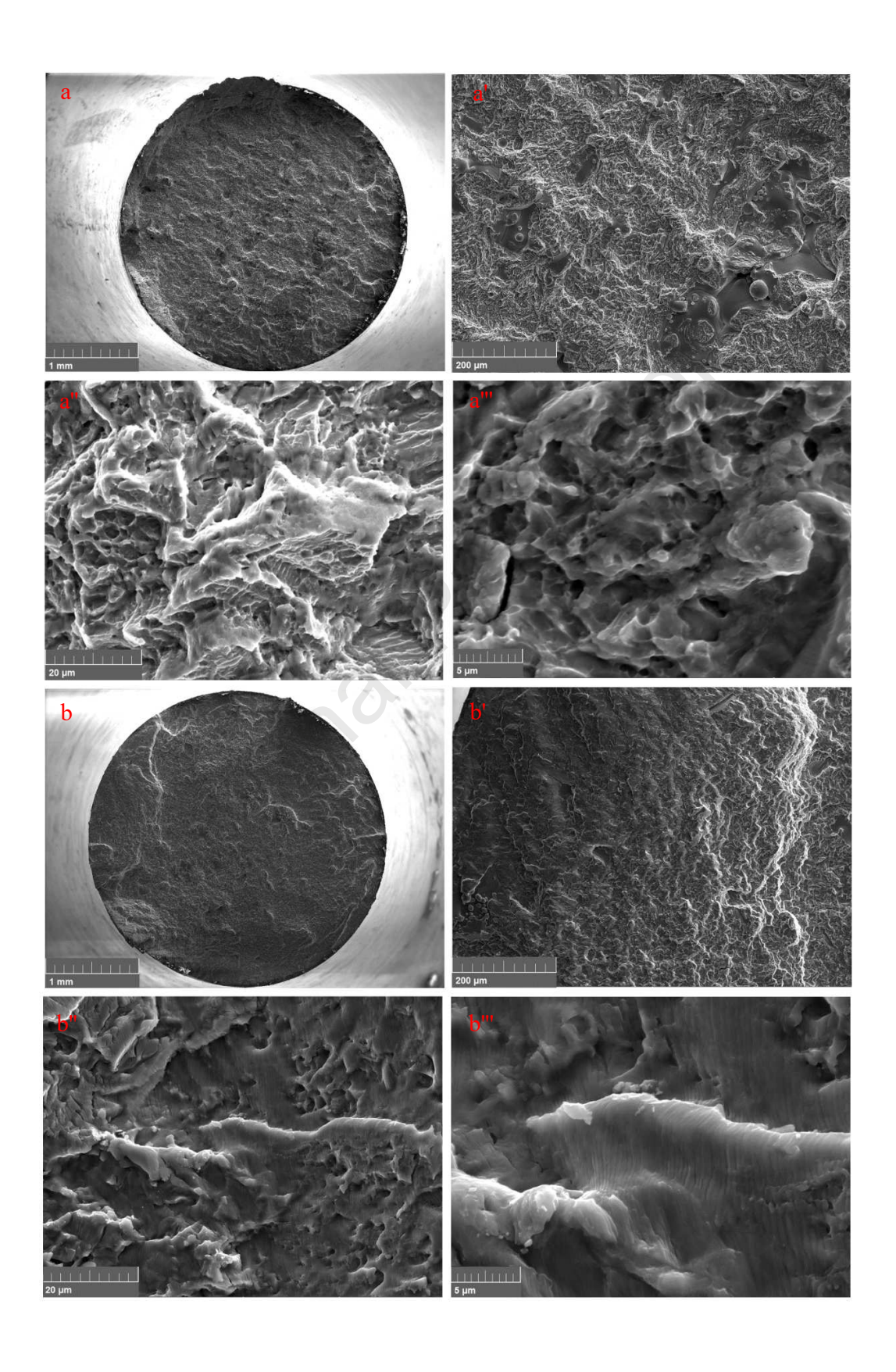


Figure 15. SE images of fractured surfaces for samples tested to fracture in HCF: (a-a") as-built + SR and (b-b") THRM. The fractographs are for samples fractured under 305 MPa and 430 MPa stress amplitudes, respectively.

#### 5. Conclusions

This paper explored the feasibility of converting acicular α microstructure of LPBF Ti64 into a wrought-like microstructure consisting of fine globular grains via THRM, a treatment that avoids an energy-intensive thermo-mechanical wrought processing or traditional powder metallurgy for achieving such structure. The results of this work show that wrought-like microstructures can indeed be produced using the THRM treatment of LPBF Ti64. The phase transformation occurring during THRM produces an ultrafine-grained lamellar α colony microstructure by homogeneous nucleation of the low temperature phases. The ultrafine-grained microstructure has enough grain boundary energy to enable formation of a fine globularized microstructure via coalescence of the  $\alpha$  colonies. While grain structure between as-built + SR and THRM samples is substantially different, crystallographic texture is remarkably similar for α-phase. Therefore, texture introduces only secondary effect on the properties. The significant grain structure changes induced by the THRM treatment cause changes in the mechanical properties. While the THRM material has lower tensile strength than the as-built + SR condition, it is significantly more ductile and, therefore, is expected to have much greater toughness. Importantly, the THRM material properties are higher than the minimums set forth by the ASTM B348 standard for annealed wrought Ti64. Furthermore, the results clearly show that it is possible to improve the fatigue strength of Ti64 by THRM. Significantly, the endurance limit improves. Moreover, the scatter in the measured fatigue strength data reduces. Performance characteristics of Ti64 can be further optimized for specific application requirements by tailoring microstructures using the LPBF and THRM processes.

## Acknowledgements

This research was sponsored by the U.S. Army Research Laboratory under the W911NF-15-2-0084 cooperative agreement and the U.S. National Science Foundation under the OIA-1757371 grant.

## **Appendix**

This appendix presents repeatability of the testing results in simple compression in Fig. A1, and drawings of the samples in Fig. A2.

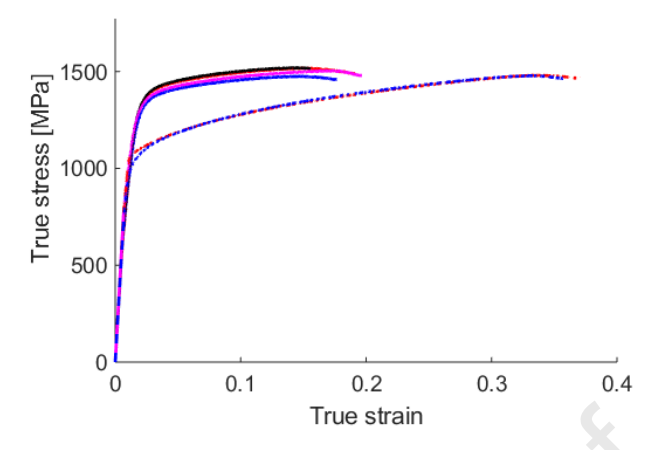


Figure A1. True stress-true strain curves showing repeatability of the testing results performed on multiple as-built + SR and THRM samples in simple compression.

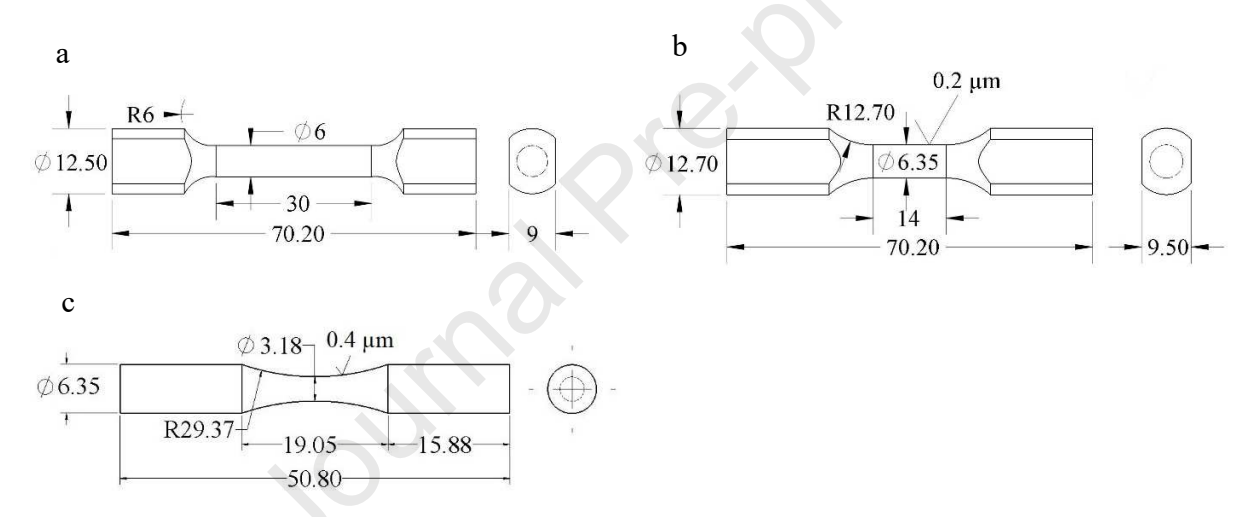


Figure A2. Drawings of (a) tensile, (b) LCF, and (c) HCF specimens with dimensions in millimeters. Compression specimens were 10 mm in height and 7.5 mm in diameter.

## Data availability

The raw/processed data required to reproduce these findings cannot be shared at this time due to technical or time limitations.

## References

[1] D. Kumar, K.B. Deepak, S.M. Muzakkir, M.F. Wani, K.P. Lijesh. Enhancing tribological performance of Ti-6Al-4V by sliding process, Tribology - Materials, Surfaces & Interfaces 12 (2018) 137-143.

- [2] H. Oguma, T. Nakamura. The effect of microstructure on very high cycle fatigue properties in Ti–6Al–4V, Scripta Materialia 63 (2010) 32-34.
- [3] J. Everaerts, B. Verlinden, M. Wevers. The influence of the alpha grain size on internal fatigue crack initiation in drawn Ti-6Al-4V wires, Procedia Structural Integrity 2 (2016) 1055-1062.
- [4] G. Lütjering, J.C. Williams. Titanium, Springer, 2003.
- [5] J.D. Paramore, Z.Z. Fang, M. Dunstan, P. Sun, B.G. Butler. Hydrogen-enabled microstructure and fatigue strength engineering of titanium alloys, Scientific Reports 7 (2017) 41444.
- [6] J.D. Paramore, Z.Z. Fang, P. Sun, M. Koopman, K.S.R. Chandran, M. Dunstan. A powder metallurgy method for manufacturing Ti-6Al-4V with wrought-like microstructures and mechanical properties via hydrogen sintering and phase transformation (HSPT), Scripta Materialia 107 (2015) 103-106.
- [7] Z.Z. Fang, P. Sun. Pathways to Optimize Performance/Cost Ratio of Powder Metallurgy Titanium A Perspective, Key Engineering Materials 520 (2012) 15-23.
- [8] V.M. Miller, S.L. Semiatin, C. Szczepanski, A.L. Pilchak. Optimization of VPSC Model Parameters for Two-Phase Titanium Alloys: Flow Stress Vs Orientation Distribution Function Metrics, Metall. Mater. Trans. A 49 (2018) 3624-3636.
- [9] I. Gibson, D. Rosen, B. Stucker. Additive Manufacturing Technologies: 3D Printing, Rapid Prototyping, and Direct Digital Manufacturing, Springer New York, 2014.
- [10] G. Tapia, A. Elwany. A review on process monitoring and control in metal-based additive manufacturing, Journal of Manufacturing Science and Engineering 136 (2014).
- [11] S. Gribbin, J. Bicknell, L. Jorgensen, I. Tsukrov, M. Knezevic. Low cycle fatigue behavior of direct metal laser sintered Inconel alloy 718, Int. J. Fatigue 93, Part 1 (2016) 156-167.
- [12] N.C. Ferreri, S. Ghorbanpour, S. Bhowmik, R. Lussier, J. Bicknell, B.M. Patterson, M. Knezevic. Effects of build orientation and heat treatment on the evolution of microstructure and mechanical properties of alloy Mar-M-509 fabricated via laser powder bed fusion, Int. J. Plast. 121 (2019) 116-133.
- [13] N.C. Ferreri, R. Pokharel, V. Livescu, D.W. Brown, M. Knezevic, J.-S. Park, M.A. Torrez, G.T. Gray. Effects of heat treatment and build orientation on the evolution of  $\epsilon$  and  $\alpha'$  martensite and strength during compressive loading of additively manufactured 304L stainless steel, Acta. Mater. 195 (2020) 59-70.
- [14] E. Herderick. Progress in Additive Manufacturing, JOM 67 (2015) 580-581.
- [15] S. Gribbin, S. Ghorbanpour, N.C. Ferreri, J. Bicknell, I. Tsukrov, M. Knezevic. Role of grain structure, grain boundaries, crystallographic texture, precipitates, and porosity on fatigue behavior of Inconel 718 at room and elevated temperatures, Mater. Charact. 149 (2019) 184-197.
- [16] D.H. Smith, J. Bicknell, L. Jorgensen, B.M. Patterson, N.L. Cordes, I. Tsukrov, M. Knezevic. Microstructure and mechanical behavior of direct metal laser sintered Inconel alloy 718, Mater. Charact. 113 (2016) 1-9.
- [17] S. Ghorbanpour, M.E. Alam, N.C. Ferreri, A. Kumar, B.A. McWilliams, S.C. Vogel, J. Bicknell, I.J. Beyerlein, M. Knezevic. Experimental characterization and crystal plasticity modeling of anisotropy, tension-compression asymmetry, and texture evolution of additively manufactured Inconel 718 at room and elevated temperatures, Int. J. Plast. 125 (2020) 63-79.
- [18] S. Ghorbanpour, M. Zecevic, A. Kumar, M. Jahedi, J. Bicknell, L. Jorgensen, I.J. Beyerlein, M. Knezevic. A crystal plasticity model incorporating the effects of precipitates in

- superalloys: Application to tensile, compressive, and cyclic deformation of Inconel 718, Int. J. Plast. 99 (2017) 162-185.
- [19] M. Thomas, T. Malot, P. Aubry, C. Colin, T. Vilaro, P. Bertrand. The prospects for additive manufacturing of bulk TiAl alloy, Materials at High Temperatures 33 (2016) pages 571-577.
- [20] S. Liu, Y.C. Shin. Additive manufacturing of Ti6Al4V alloy: A review, Mater. Des. 164 (2019) 107552.
- [21] A.M. Beese, B.E. Carroll. Review of Mechanical Properties of Ti-6Al-4V Made by Laser-Based Additive Manufacturing Using Powder Feedstock, JOM 68 (2016) 724-734.
- [22] S. Leuders, M. Thöne, A. Riemer, T. Niendorf, T. Tröster, H.A. Richard, H.J. Maier. On the mechanical behaviour of titanium alloy TiAl6V4 manufactured by selective laser melting: Fatigue resistance and crack growth performance, International Journal of Fatigue 48 (2013) 300-307.
- [23] B. Vrancken, L. Thijs, J.-P. Kruth, J. Van Humbeeck. Heat treatment of Ti6Al4V produced by Selective Laser Melting: Microstructure and mechanical properties, JAllC 541 (2012) 177-185.
- [24] J. Yang, H. Yu, J. Yin, M. Gao, Z. Wang, X. Zeng. Formation and control of martensite in Ti-6Al-4V alloy produced by selective laser melting, Mater. Des. 108 (2016) 308-318.
- [25] A.H. Chern, P. Nandwana, T. Yuan, M.M. Kirka, R.R. Dehoff, P.K. Liaw, C.E. Duty. A review on the fatigue behavior of Ti-6Al-4V fabricated by electron beam melting additive manufacturing, Int. J. Fatigue 119 (2019) 173-184.
- [26] S. Beretta, S. Romano. A comparison of fatigue strength sensitivity to defects for materials manufactured by AM or traditional processes, Int. J. Fatigue 94 (2017) 178-191.
- [27] C. de Formanoir, S. Michotte, O. Rigo, L. Germain, S. Godet. Electron beam melted Ti–6Al–4V: Microstructure, texture and mechanical behavior of the as-built and heat-treated material, Mater. Sci. Eng. A 652 (2016) 105-119.
- [28] W.E. Frazier. Metal additive manufacturing: a review, J. Mater. Eng. Perform. 23 (2014) 1917-1928.
- [29] L. Denti, E. Bassoli, A. Gatto, E. Santecchia, P. Mengucci. Fatigue life and microstructure of additive manufactured Ti6Al4V after different finishing processes, Mater. Sci. Eng. A 755 (2019) 1-9.
- [30] H. Masuo, Y. Tanaka, S. Morokoshi, H. Yagura, T. Uchida, Y. Yamamoto, Y. Murakami. Influence of defects, surface roughness and HIP on the fatigue strength of Ti-6Al-4V manufactured by additive manufacturing, Int. J. Fatigue 117 (2018) 163-179.
- [31] Z.Z. Fang, P. Sun, J. Paramore, H. Wang, M. Koopman, L. Yang. Powder metallurgy methods for the production of fine and ultrafine grain Ti and Ti alloys. vol. 9,816,157 B2. United States, 2017.
- [32] J.D. Paramore, B.G. Butler, M.K. Dunstan, J.P. Ligda, Z.Z. Fang. Thermo-hydrogen refinement of microstructure of titanium materials, Patent Application US 2019/0106777 A1. 2019.
- [33] D. Eylon, F. Froes, S. Abkowitz. ASM Handbook Vol. 7: Powder Metal Technologies and Applications. Materials Park, OH: ASM International, 1998.
- [34] O.M. Ivasishin, D.G. Savvakin, F.H. Froes, K.A. Bondareva. Synthesis of Alloy Ti 6Al 4V with Low Residual Porosity by a Powder Metallurgy Method, Powder Metallurgy and Metal Ceramics 41 (2002) 382-390.
- [35] G. Lütjering, J.C. Williams. Titanium, Springer, Berlin Heidelberg New York, 2007.

- [36] H.-C. Kou, H.-L. Zhang, Y.-D. Chu, D. Huang, H. Nan, J.-S. Li. Microstructure Evolution and Phase Transformation of Ti–6.5Al–2Zr–Mo–V Alloy During Thermohydrogen Treatment, Acta Metallurgica Sinica (English Letters) 28 (2015) 505-513.
- [37] Y. Zong, K. Wu. Thermo hydrogen treatment for microstructure refinement and mechanical properties improvement of Ti-6Al-4V alloy, Mater. Sci. Eng. A 703 (2017) 430-437.
- [38] P. Sun, Z.Z. Fang, M. Koopman, J. Paramore, K.R. Chandran, Y. Ren, J. Lu. An experimental study of the (Ti–6Al–4V)–xH phase diagram using in situ synchrotron XRD and TGA/DSC techniques, Acta. Mater. 84 (2015) 29-41.
- [39] P. Sun, Z.Z. Fang, M. Koopman, Y. Xia, J. Paramore, K.R. Chandran, Y. Ren, J. Lu. Phase transformations and formation of ultra-fine microstructure during hydrogen sintering and phase transformation (HSPT) processing of Ti-6Al-4V, Metall. Mater. Trans. A 46 (2015) 5546-5560.
- [40] M. Dunstan, Z.Z. Fang, M. Koopman, J. Paramore. Powder Metallurgy Ti-6Al-4V Alloy with Wrought-like Microstructure and Mechanical Properties by Hydrogen Sintering. Key Engineering Materials, vol. 704: Trans Tech Publ, 2016. p.3-14.
- [41] ASTM. B348-10: Standard Specification for Titanium and Titanium Alloy Bars and Billets. West Conshohocken, PA, 2010. doi:10.1520/B0348.
- [42] G. Welsch, R. Boyer, E. Collings. Materials properties handbook: titanium alloys, ASM international, 1993.
- [43] B.M. Patterson, J.P. Escobedo-Diaz, D. Dennis-Koller, E. Cerreta. Dimensional quantification of embedded voids or objects in three dimensions using X-ray tomography, Microscopy and Microanalysis 18 (2012) 390-398.
- [44] A.D. Kudzal, B.A. McWilliams, J. Taggart-Scarff, M. Knezevic. Fabrication of a low alloy ultra-high strength (>1500 MPa yield) steel using powder bed fusion additive manufacturing, Mater. Sci. Eng. A 770 (2020) 138512.
- [45] D. Kim, K. Son, D. Sung, Y. Kim, W. Chung. Effect of added ethanol in ethylene glycol–NaCl electrolyte on titanium electropolishing, Corrosion Science 98 (2015) 494-499.
- [46] N.C. Ferreri, D.J. Savage, M. Knezevic. Non-acid, alcohol-based electropolishing enables high-quality electron backscatter diffraction characterization of titanium and its alloys: Application to pure Ti and Ti-6Al-4V, Mater. Charact. 166 (2020) 110406.
- [47] H.-R. Wenk, L. Lutterotti, S. Vogel. Texture analysis with the new HIPPO TOF diffractometer, Nuclear Instruments and Methods in Physics Research Section A: Accelerators, Spectrometers, Detectors and Associated Equipment 515 (2003) 575-588.
- [48] H.-R. Wenk, L. Lutterotti, S. Vogel. Rietveld texture analysis from TOF neutron diffraction data, Powder Diffraction 25 (2010) 283-296.
- [49] ASTM E8/E8M-15a. Standard Test Methods for Tension Testing of Metallic Materials. West Conshohocken, PA: ASTM International, 2015.
- [50] S. Ghorbanpour, B.A. McWilliams, M. Knezevic. Low-cycle fatigue behavior of rolled WE43-T5 magnesium alloy, Fatigue & Fracture of Engineering Materials & Structures 42 (2019) 1357-1372.
- [51] M. Knezevic, A. Levinson, R. Harris, R.K. Mishra, R.D. Doherty, S.R. Kalidindi. Deformation twinning in AZ31: Influence on strain hardening and texture evolution, Acta. Mater. 58 (2010) 6230-6242.
- [52] M. Jahedi, B.A. McWilliams, P. Moy, M. Knezevic. Deformation twinning in rolled WE43-T5 rare earth magnesium alloy: Influence on strain hardening and texture evolution, Acta. Mater. 131 (2017) 221-232.

- [53] ASTM E606/E606M-12. Standard Test Method for Strain-Controlled Fatigue Testing. West Conshohocken, PA: ASTM International, 2012.
- [54] ASTM International. E466-15 Standard Practice for Conducting Force Controlled Constant Amplitude Axial Fatigue Tests of Metallic Materials. . ASTM, 2015.
- [55] S. Ghorbanpour, B.A. McWilliams, M. Knezevic. Effect of hot working and aging heat treatments on monotonic, cyclic, and fatigue behavior of WE43 magnesium alloy, Mater. Sci. Eng. A 747 (2019) 27-41.
- [56] S. Ghorbanpour, B.A. McWilliams, M. Knezevic. Effects of environmental temperature and sample pre-straining on high cycle fatigue strength of WE43-T5 magnesium alloy, Int. J. Fatigue 141 (2020) 105903.
- [57] J. Günther, D. Krewerth, T. Lippmann, S. Leuders, T. Tröster, A. Weidner, H. Biermann, T. Niendorf. Fatigue life of additively manufactured Ti–6Al–4V in the very high cycle fatigue regime, Int. J. Fatigue 94 (2017) 236-245.
- [58] A.L. Pilchak, T.F. Broderick. Evidence of a Massive Transformation in a Ti-6Al-4V Solid-State Weld?, JOM 65 (2013) 636-642.
- [59] W. Burgers. On the process of transition of the cubic-body-centered modification into the hexagonal-close-packed modification of zirconium, Physica 1 (1934) 561-586.
- [60] S. Ankem, H. Margolin. A rationalization of stress-strain behavior of two-ductile phase alloys, MTA 17 (1986) 2209-2226.
- [61] Z. Zhao, Q. Wang, H. Wang, J. Liu, R. Yang. Determining the orientation of parent  $\beta$  grain from one  $\alpha$  variant in titanium alloys, Journal of Applied Crystallography 51 (2018) 1125-1132.
- [62] N. Stanford, P. Bate. Crystallographic variant selection in Ti–6Al–4V, Acta. Mater. 52 (2004) 5215-5224.
- [63] M. Knezevic, S.R. Kalidindi. Fast computation of first-order elastic-plastic closures for polycrystalline cubic-orthorhombic microstructures, Comput. Mater. Sci. 39 (2007) 643-648.
- [64] M. Humbert, F. Wagner, H. Moustahfid, C. Esling. Determination of the Orientation of a Parent  $\beta$  Grain from the Orientations of the Inherited  $\alpha$  Plates in the Phase Transformation from Body-Centred Cubic to Hexagonal Close Packed, Journal of Applied Crystallography 28 (1995) 571-576.
- [65] M. Humbert, H. Moustahfid, F. Wagner, M.J. Philippe. Evaluation of the high temperature texture of the  $\beta$  phase of a TA6V sample from the individual orientations of grains of the low temperature  $\alpha$  phase, Scripta Metallurgica et Materialia 30 (1994) 377-382.
- [66] M.G. Glavicic, P.A. Kobryn, T.R. Bieler, S.L. Semiatin. A method to determine the orientation of the high-temperature beta phase from measured EBSD data for the low-temperature alpha phase in Ti-6Al-4V, Mater. Sci. Eng. A 346 (2003) 50-59.
- [67] S.R. Kalidindi, H.K. Duvvuru, M. Knezevic. Spectral calibration of crystal plasticity models, Acta. Mater. 54 (2006) 1795-1804.
- [68] Z.B. Zhao, Q.J. Wang, H. Wang, J.R. Liu, R. Yang. Determining the orientation of parent  $\beta$  grain from one  $\alpha$  variant in titanium alloys, Journal of Applied Crystallography 51 (2018) 1125-1132.
- [69] C. Cayron. Groupoid of orientational variants, Acta Crystallographica Section A: Foundations of Crystallography 62 (2006) 21-40.
- [70] A.L. Pilchak, J.C. Williams. Microstructure and Texture Evolution during Friction Stir Processing of Fully Lamellar Ti-6Al-4V, Metall. Mater. Trans. A 42 (2011) 773-794.

- [71] N.C. Ferreri, S.C. Vogel, M. Knezevic. Determining volume fractions of  $\gamma$ ,  $\gamma'$ ,  $\gamma''$ ,  $\delta$ , and MC-carbide phases in Inconel 718 as a function of its processing history using an advanced neutron diffraction procedure, Mater. Sci. Eng. A 781 (2020) 139228.
- [72] I.A. Riyad, W.G. Feather, E. Vasilev, R.A. Lebensohn, B.A. McWilliams, A.L. Pilchak, M. Knezevic. Modeling the role of local crystallographic correlations in microstructures of Ti-6Al-4V using a correlated structure visco-plastic self-consistent polycrystal plasticity formulation, Acta. Mater. 203 (2021) 116502.
- [73] J. Bauschinger. Über die Veränderung der Elasticitätsgrenze und Festigkeit des Eisen und Stahls durch Strecken und Quetschen, durch Erwarmen und Abkühlen und durch oftmal wiederholte Beanspruchung, Mitteilungen aus dem mechanisch-technischen Laboratorium der k. polytechnischen Schule (1886) 1877-1836.
- [74] M. Zecevic, M. Knezevic. A dislocation density based elasto-plastic self-consistent model for the prediction of cyclic deformation: Application to Al6022-T4, Int. J. Plast. 72 (2015) 200-217.
- [75] M. Zecevic, M. Knezevic. Latent hardening within the elasto-plastic self-consistent polycrystal homogenization to enable the prediction of anisotropy of AA6022-T4 sheets, Int. J. Plast. 105 (2018) 141-163.
- [76] M. Zecevic, M. Knezevic. An implicit formulation of the elasto-plastic self-consistent polycrystal plasticity model and its implementation in implicit finite elements, Mechanics of Materials 136 (2019) 103065.
- [77] M. Zecevic, Y.P. Korkolis, T. Kuwabara, M. Knezevic. Dual-phase steel sheets under cyclic tension–compression to large strains: Experiments and crystal plasticity modeling, J. Mech. Phys. Solids 96 (2016) 65-87.
- [78] A. Eghtesad, M. Knezevic. A full-field crystal plasticity model including the effects of precipitates: Application to monotonic, load reversal, and low-cycle fatigue behavior of Inconel 718, Mater. Sci. Eng. A (2020) 140478.
- [79] A. Eghtesad, M. Knezevic. High-performance full-field crystal plasticity with dislocation-based hardening and slip system back-stress laws: Application to modeling deformation of dual-phase steels, J. Mech. Phys. Solids 134 (2020) 103750.
- [80] W. Roberts, J. Gong, A.J. Wilkinson, E. Tarleton. Tension—compression asymmetry of c+a slip in Ti–6Al, Scr. Mater. 178 (2020) 119-123.
- [81] T. Neeraj †, M.F. Savage, J. Tatalovich, L. Kovarik, R.W. Hayes, M.J. Mills. Observation of tension–compression asymmetry in  $\alpha$  and  $\alpha/\beta$  titanium alloys, Philosophical Magazine 85 (2005) 279-295.
- [82] M.A.W. Lowden, W.B. Hutchinson. Texture strengthening and strength differential in titanium-6Al-4V, MTA 6 (1975) 441.
- [83] R. Ding, J. Gong, A.J. Wilkinson, I.P. Jones. 〈c+a〉 Dislocations in deformed Ti–6Al–4V micro-cantilevers, Acta. Mater. 76 (2014) 127-134.
- [84] D.J. Savage, I.J. Beyerlein, M. Knezevic. Coupled texture and non-Schmid effects on yield surfaces of body-centered cubic polycrystals predicted by a crystal plasticity finite element approach, International Journal of Solids and Structures 109 (2017) 22-32.
- [85] D.J. Savage, N. Chandola, O. Cazacu, B.A. McWilliams, M. Knezevic. Validation of recent analytical dilatational models for porous polycrystals using crystal plasticity finite element models with Schmid and non-Schmid activation laws, Mechanics of Materials 126 (2018) 148-162.

- [86] M. Knezevic, I.J. Beyerlein, M.L. Lovato, C.N. Tomé, A.W. Richards, R.J. McCabe. A strain-rate and temperature dependent constitutive model for BCC metals incorporating non-Schmid effects: Application to tantalum—tungsten alloys, Int. J. Plast. 62 (2014) 93-104.
- [87] M. Zecevic, M. Knezevic. A new visco-plastic self-consistent formulation implicit in dislocation-based hardening within implicit finite elements: Application to high strain rate and impact deformation of tantalum, Computer Methods in Applied Mechanics and Engineering 341 (2018) 888-916.
- [88] M. Knezevic, M. Zecevic, I.J. Beyerlein, A. Bhattacharyya, R.J. McCabe. Predicting Texture Evolution in Ta and Ta-10W Alloys Using Polycrystal Plasticity, JOM 67 (2015) 2670-2674.
- [89] T. Neeraj, M.F. Savage, J. Tatalovich, L. Kovarik, R.W. Hayes, M.J. Mills. Observation of tension–compression asymmetry in  $\alpha$  and titanium alloys, Philosophical Magazine 85 (2005) 279-295.
- [90] B. Franco, J. Ma, B. Loveall, G. Tapia, K. Karayagiz, J. Liu, A. Elwany, R. Arroyave, I. Karaman. A sensory material approach for reducing variability in additively manufactured metal parts, Sci. Rep. 7 (2017) 1-12.
- [91] S. Suri, G.B. Viswanathan, T. Neeraj, D.H. Hou, M.J. Mills. Room temperature deformation and mechanisms of slip transmission in oriented single-colony crystals of an  $\alpha/\beta$  titanium alloy, Acta. Mater. 47 (1999) 1019-1034.
- [92] J.R. Seal, M.A. Crimp, T.R. Bieler, C.J. Boehlert. Analysis of slip transfer and deformation behavior across the  $\alpha/\beta$  interface in Ti–5Al–2.5Sn (wt.%) with an equiaxed microstructure, Mater. Sci. Eng. A 552 (2012) 61-68.
- [93] Y. Guo, T.B. Britton, A.J. Wilkinson. Slip band–grain boundary interactions in commercial-purity titanium, Acta. Mater. 76 (2014) 1-12.
- [94] M. Jahedi, M. Knezevic, M. Paydar. High-Pressure Double Torsion as a Severe Plastic Deformation Process: Experimental Procedure and Finite Element Modeling, J. Mater. Eng. Perform. 24 (2015) 1471-1482.
- [95] G. Kasperovich, J. Hausmann. Improvement of fatigue resistance and ductility of TiAl6V4 processed by selective laser melting, Journal of Materials Processing Technology 220 (2015) 202-214.
- [96] A. Fatemi, R. Molaei, S. Sharifimehr, N. Phan, N. Shamsaei. Multiaxial fatigue behavior of wrought and additive manufactured Ti-6Al-4V including surface finish effect, Int. J. Fatigue 100 (2017) 347-366.
- [97] S. Leuders, M. Vollmer, F. Brenne, T. Tröster, T. Niendorf. Fatigue strength prediction for titanium alloy TiAl6V4 manufactured by selective laser melting, Metall. Mater. Trans. A 46 (2015) 3816-3823.
- [98] E.S. Hodge, R.F. Tavenner. Method for pneumatic isostatic processing of a workpiece. Google Patents, 1998.

## Journal Pre-proof

Declaration of interests					
oxtimes The authors declare that they have no known competing financial interests or personal relationships that could have appeared to influence the work reported in this paper.					
☐ The authors declare the following financial interests/personal as potential competing interests:	relationships which may be considered				
	300 <sup>5</sup>				